Energy Storage Materials 4 (2016) 103–129

Contents lists available at ScienceDirect

Energy Storage Materials

journal homepage: www.elsevier.com/locate/ensm

Emerging non-lithium ion batteries

Yanrong Wang [a,1], Renpeng Chen [a,1], Tao Chen [a], Hongling Lv [a], Guoyin Zhu [a], Lianbo Ma [a], Caixing Wang [a], Zhong Jin [a,*], Jie Liu [a,b,**]

[a] Key Laboratory of Mesoscopic Chemistry of MOE and Collaborative Innovation Center of Chemistry for Life Sciences, School of Chemistry and Chemical Engineering, Nanjing University, Nanjing 210093, China
[b] Department of Chemistry, Duke University, Durham, NC 27708, USA

ARTICLE INFO

Article history:
Received 30 December 2015
Received in revised form
4 April 2016
Accepted 7 April 2016
Available online 13 April 2016

Keywords:
Electrochemical energy storage
Non-lithium ion batteries
Rechargeable secondary batteries
Cathode and anode materials
Electrolytes

ABSTRACT

Li-ion batteries have dominated the field of electrochemical energy storage for the last 20 years. It still remains to be one of the most active research fields. However, there are difficult problems still surrounding lithium ion batteries, such as high cost, unsustainable lithium resource and safety issues. Rechargeable batteries base on alternative metal elements (Na, K, Mg, Ca, Zn, Al, *etc.*) can provide relatively high power density and energy density using abundant, low-cost materials. Therefore, non-lithium ion batteries are regarded as promising candidates to partially replace lithium ion batteries in near future. In recent years, the research on non-lithium rechargeable batteries is progressing rapidly, but many fundamental and technological obstacles remain to be overcome. Here we provide an overview of the current state of non-lithium rechargeable batteries based on monovalent metal ions (Na^+ and K^+) and multivalent metal ions (Mg^{2+}, Ca^{2+}, Zn^{2+} and Al^{3+}). The needs and possible choices of superior electrode materials and compatible electrolytes beneficial for ion transport were emphatically discussed in this review.

Contents

Abbreviations: AIBs, aluminum ion batteries; CIBs, calcium ion batteries; LIBs, lithium ion batteries; MIBs, magnesium ion batteries; NASICON, sodium super ionic conductor; PBAs, Prussian blue analogues; PIBs, potassium ion batteries; SEI, solid-electrolyte interface; SHE, standard hydrogen electrode; SIBs, sodium ion batteries; XRD, X-ray diffraction; ZIBs, zinc ion batteries

* Corresponding author.
** Corresponding authors at: Key Laboratory of Mesoscopic Chemistry of MOE and Collaborative Innovation Center of Chemistry for Life Sciences, School of Chemistry and Chemical Engineering, Nanjing University, Nanjing 210093, China.
E-mail addresses: zhongjin@nju.edu.cn (Z. Jin), j.liu@duke.edu (J. Liu).
[1] Both authors contributed equally to this work.

http://dx.doi.org/10.1016/j.ensm.2016.04.001
2405-8297/

1. Introduction

High-efficiency electrochemical energy storage devices have become an urgent demand over the past few decades along with the rapid increase of global energy consumption, the drain of fossil fuels and the aggravation of environmental problems [1–3]. Significant attention has been drawn to the research of alternative eco-friendly energy systems based on renewable resources to alleviate these crises [4–6]. The secondary batteries, especially rechargeable lithium-ion batteries (LIBs), are capable of storing and releasing electric energy for many times [7,8]. While the application of LIBs as a major power source in portable devices and electric vehicles is rapidly expanding, the current LIB technology is still facing several difficult challenges, such as resource limitation, high cost, potential safety issue and insufficient energy density [9,10]. In particular, the rarity and uneven distribution of global lithium reserves results in rising cost [11]. Graphite has long been used as anode material in commercial LIBs with a low operating voltage closed to 0 V *vs.* Li/Li^{+}, which has a beneficial effect on the energy density, but also lead to the formation of potentially risky lithium dendrite [12]. The dendritic deposition of lithium metal may result in short circuits leading to internal overheating and even flaming [13,14]. Furthermore, it is imperative to develop rechargeable batteries with higher energy density for electric vehicles to get better mileage. The state-of-art commercial LIBs are difficult to satisfy the practical needs [15,16]. Even though lithium metal has a high theoretical volumetric capacity of 2062 mA h mL^{-1} and a highly negative reduction potential of −3.04 V *vs.* standard hydrogen electrode (SHE), as shown in Table 1, these unresolved problems motivated researchers to make considerable effort to develop new types of rechargeable batteries with high sustainability and performances beyond LIBs.

A possible solution for overcoming the disadvantages of LIBs would be the non-lithium batteries based on alternative metal ions [17], such as alkali metals (Na^{+} and K^{+}), alkaline earth metals (Mg^{2+} and Ca^{2+}), group IIIA metal (Al^{3+}) and transition metal (Zn^{2+}). Non-lithium ion based batteries with high energy density, good environmental benignity and low cost have great potentialities for energy storage in future [18–23].

Secondary batteries based on monovalent alkali metal ions, including Na^{+} and K^{+}, have the advantages of high abundance and low price. Nonetheless, several obstacles still need to be overcome before these batteries can become a practical, commercial reality. The challenges include how to improve the insufficient cycle life and how to design new anode and cathode materials with high specific energy capacity [24–26]. Other rechargeable batteries based on multivalent metal ions (such as Mg^{2+}, Ca^{2+}, Zn^{2+} and Al^{3+}) could transfer more electrons in a single redox couple, hence possibly helpful to obtain high volumetric energy density that is desirable for portable devices [17,27,28]. In addition, multivalent metal anodes do not appear to be troubled by dendrite formation to the same degree as lithium metal anodes. Moreover, air and moisture exposure is a much lesser safety problem for multivalent metal ion batteries compared to LIBs [5]. However, rechargeable batteries based on multivalent metal ions also need to overcome several difficulties before usage in practical applications. The biggest challenge is the lack of suitable electrode materials in which multivalent metal ions can diffuse with fast kinetics and the lack of high-voltage electrolytes compatible with electrodes [29,30].

In this review, we summarized the recent progresses and hurdles encountered by secondary batteries based on non-lithium ions. We expect that this review may provide some new insights into the further development of rechargeable batteries beyond LIBs and reveal their immense potential in electrochemical energy storage aspect.

Table 1
Theoretical capacities, reduction potential and effective ionic radius of various metals.

Species	Volumetric capacity (mA h mL^{-1})	Specific capacity (mA h g^{-1})	Reduction potential (*V vs.* SHE)	Effective ionic radius (Å)
Li	2026	3861	−3.04	0.76
Na	1128	1165	−2.71	1.02
K	591	685	−2.93	1.38
Mg	3833	2205	−2.37	0.72
Ca	2073	1337	−2.87	1.00
Zn	5851	820	−2.20	0.74
Al	8040	2980	−1.67	0.54

2. Sodium ion batteries

Sodium ion batteries (SIBs) were originally developed in the late 1980s, approximately in the same time period as LIBs [31]. In recent years, SIBs have drawn increasing attention for large-scale energy storage, because of the natural abundance, low cost and environmental benignity of sodium [4,32–34]. Worldwide research on SIBs is now flourishing, and SIBs are considered as one of the most appealing alternative rechargeable batteries to LIBs. SIBs have a theoretical specific capacity of 1165 mA h g^{-1} with a negative reduction potential of −2.71 V *vs.* SHE (Table 1). Since the size of Na^{+} (radius ~1.02 Å) is larger than Li^{+}, most materials don't have sufficiently big interstitial space to host Na^{+}, leading to sluggish diffusion kinetics of Na^{+} in electrode materials [9]. Therefore, a great challenge for developing SIBs is to find appropriate electrode materials capable of hosting Na^{+} with high capacity and fast diffusion kinetics [35]. Up to now, many different electrode materials have been synthesized, but the capacities and the rate performances of assembled SIBs are still not satisfactory for practical applications.

2.1. Cathode materials

For SIBs, cathode materials with high voltage (>2.0 V *vs.* Na/Na^+) are desired for greater energy density. In contrast to anodes, the search for cathode materials in SIBs is relatively fruitful, including many sodium-based transition metal oxides, hexacyanoferrates, poly-anionic compounds and so on. In this review, we have separated the recently-reported cathode materials into several groups according to their structural differences, as shown in Table 2. Their advantage and disadvantages are compared.

2.1.1. Sodium-based transition metal oxides

Sodium-based layered metal oxides, $Na_xT_MO_2$ (T_M=V [36], Cr [37], Mn [38], Fe [39], Co [40], or Ni [41], *etc.*), have been extensively investigated for cathodes of SIBs since 1980 s. The sodium layered oxides can be synthesized in O3 (ABCABC stacking), P2 (ABBA stacking) and P3 (ABBCCA stacking) phases (O=octahedral and P=prismatic). Most of the layered NaT_MO_2 are composed of T_MO_6 octahedrons and sodium coordination polyhedrons.

Recently, Myung et al. reported the preparation of layered O3-type $NaCrO_2$ with good capacity retention, high rate capability via an emulsion drying method [42]. Carbon-modified $NaCrO_2$ cathodes have much higher electrical conductivity ($\sim 10^{-1}$ S cm^{-1}) than that of bare $NaCrO_2$ (8×10^{-5} S cm^{-1}), which can accelerate the reversible insertion/extraction of sodium ions and the facile complementary redox reactions of Cr^{4+}/Cr^{3+} couple. The chemical diffusion of Na^+ in $Na_{0.5}CrO_2$ with the monoclinic P3 structure and higher conductivity ($\sim 10^{-9}$ S cm^{-1}) at the end of charging is much faster than that in $Na_{0.92}CrO_2$ with hexagonal O3 structure ($\sim 10^{-13}$ S cm^{-1}), owing to the larger interlayer distance of $Na_{0.5}CrO_2$. The phase transition occurs in a sequence of original hexagonal O3 → monoclinic O3 → monoclinic P3 during the charge process and occurs in a reverse sequence during the discharge process. The 3.4% carbon-modified $NaCrO_2$ has a good capacity retention of about 90% after 300 cycles, and delivers high capacity of 106 mA h g^{-1} at a current density of 5.5 A g^{-1}. A high-rate capacity of 99 mA h g^{-1} is obtained at 150 C, corresponding to a very short discharge time of 27 s.

Anti-P2-type $Na_{0.5}NbO_2$, a new layered oxide composed of unique NbO_6 trigonal prisms and NaO_6 octahedrons was recently reported [43]. Its lattice shrinks as sodium ions are intercalated and expands as sodium ions are deintercalated (a negative volume or strain effect), owing to the increased interlayer (Na–O) interaction and the decreased Nb–Nb and Nb–O interaction in the O–Nb–O slab upon Na intercalation (Fig. 1a). Moreover, $Na_{0.5}NbO_2$ exhibits high structural stability and good rate performance as a cathodic electrode of SIBs. These special features make $Na_{0.5}NbO_2$ a good "volume buffer" as compensation for the *positive-strain* electrode materials to achieve high energy density and long cycling life. A capacity of 68.3 mA h g^{-1} after 1500 cycles at 170 mA g^{-1} is achieved for anti-P2 $Na_{0.5}NbO_2$ cathodes with an average capacity fading of $\sim$0.0047% per cycle (Fig. 1b). When the current density is increased to 620 mA g^{-1}, a reversible storage capacity of 45 mA h g^{-1} is obtained, referring to 64% capacity retention. The rate performance is mainly attributed to its native high conductivity (Fig. 1c).

Mai et al. have synthesized novel hierarchical zigzag structured $Na_{1.25}V_3O_8$ nanowires *via* a topotactic intercalation method [44].

Table 2
Electrochemical properties of typical cathode materials for SIBs reported in the literature.

Electrode material	Ref.	Reversible capacity (mA h g^{-1})	Current density (mA g^{-1} or C)	Capacity retention
1. Sodium-based transition metal oxides				
Carbon-modified $NaCrO_2$	[42]	106	5500	90% after 300 cycles at 20 mA g^{-1}
$Na_{0.5}NbO_2$	[43]	68.3	170	93% after 1500 cycles at 170 mA g^{-1}
$Na_{1.25}V_3O_8$	[44]	105.9	1000	87% after 1000 cycles at 1 A g^{-1}
$Na_3Ni_2SbO_6$	[47]	133	C/50	70% after 500 cycles at 2 C
$Na[Ni_{0.4}Fe_{0.2}Mn_{0.2}Ti_{0.2}]O_2$	[48]	145	0.1 C	84% after 200 cycles at 0.1 C
$Na_{0.61}[Mn_{0.27}Fe_{0.34}Ti_{0.39}]O_2$	[49]	90	C/5	90% after 100 cycles at C/5
$NaNi_{1/3}Mn_{1/3}Co_{1/3}O_2$	[50]	120	C/10	~100% after 50 cycles at C/10
$Na_{0.67}[Mn_{0.65}Ni_{0.15}Co_{0.15}Al_{0.05}]O_2$	[51]	141	20	95% after 50 cycles at 20 mA g^{-1}
$Na_{0.8}Li_{0.4}Ni_{0.15}Mn_{0.55}Co_{0.1}O_2$	[52]	138	15	80% after 100 cycles at 75 mA g^{-1}
$Na[Ni_{0.6}Co_{0.05}Mn_{0.35}]O_2$	[53]	157	15	80% after 300 cycles at 0.1 C
2. Prussian blue analogues				
$Na_2Mn^{II}[Mn^{II}(CN)_6]$	[55]	134	1/20 C	90% after 30 cycles at 1/20 C
(Cu^{II}–N≡C–$Fe^{III/II}$) cathode and (Mn^{II}–N≡C–$Mn^{III/II}$) anode	[59]	~23	10 C	~100% after 1000 cycles at 10 C
$Na_{0.61}Fe[Fe(CN)_6]_{0.94}$	[60]	170	25	~100% after 160 cycles at 25 mA g^{-1}
$Na_{1.72}MnFe(CN)_6$	[61]	209	40	75% after 100 cycles at 2 C
$Na_{1.70}FeFe(CN)_6$	[62]	120.7	200	75% after 100 cycles at 200 mA g^{-1}
3. Phosphates, fluorophosphates and pyrophosphates				
Maricite $NaFePO_4$	[66]	142	C/20	95% after 200 cycles at C/20
$NaFePO_4$	[67]	152	0.1 C	95% after 300 cycles at 0.1 C
C-$Na_3V_2(PO_4)_3$	[68]	114	1 C	50% after 30,000 cycles at 40 C
$Na_3V_2(PO_4)_3$	[69]	103	10 C	
$Na_3V_2(PO_4)_3$	[72]	112	0.5 C	54% after 20000 cycles at 30 C
$Na_{1.5}VPO_{4.8}F_{0.7}$	[75]	155.6	12.97	84% after 500 cycles at 1 C
$Na_2FeP_2O_7$	[77]	90	C/10	~100% after 30 cycles at C/10
$Na_2MnP_2O_7$	[79]	80	C/5	96% after 30 cycles at C/5
$Na_4Co_3(PO_4)_2P_2O_7$	[80]	95	0.2 C	93% after 50 cycles at 0.2 C
4. Sulfates				
$Na_2Fe(SO_4)_2\cdot 2H_2O$	[83]	70	C/20	86% after 30 cycles at C/20
$Na_2Fe_2(SO_4)_3$	[84]	102	C/20	86% after 30 cycles at C/20

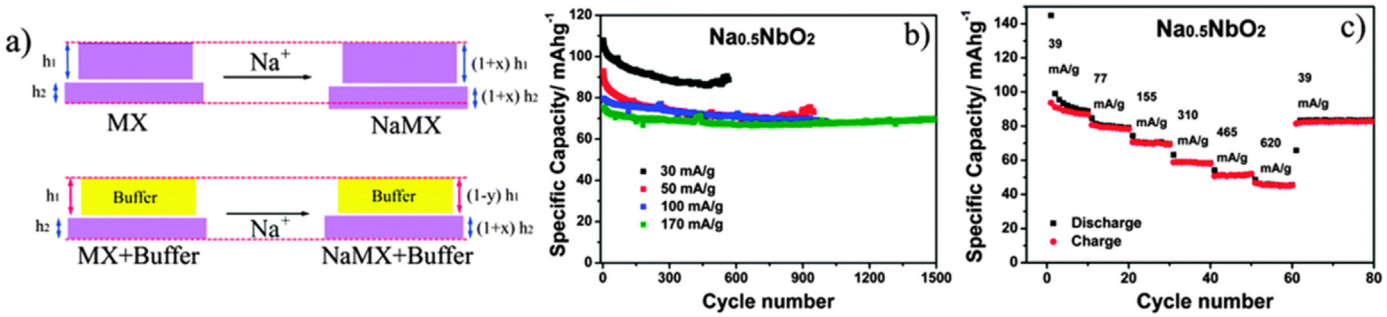

Fig. 1. Schematic illustration of (a) volume buffer, (b) cycling stability and (c) rate performance of anti-P2 $Na_{0.5}NbO_2$ cathodes [43].

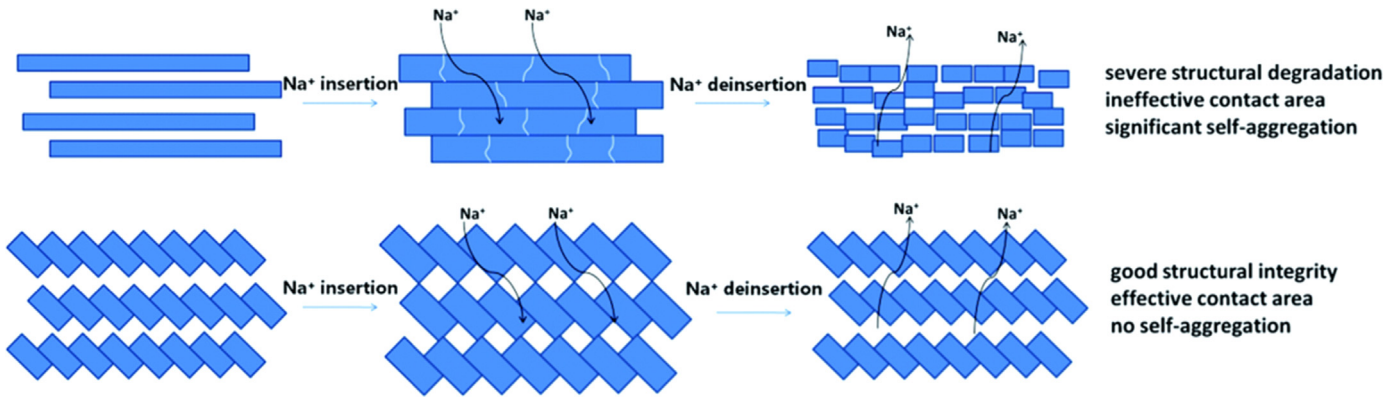

Fig. 2. Schematic illustration of Na^+ diffusion process for normal $Na_{1.25}V_3O_8$ nanowires (up) and hierarchical zigzag $Na_{1.25}V_3O_8$ nanowires (down) [44].

The unique morphology provides an increased electrode–electrolyte contact area, better strain accommodation, prevent self-aggregation and also shorten Na ion diffusion path (Fig. 2). It was demonstrated that the monoclinic $Na_{1.25}V_3O_8$ nanowires exhibited a high capacity of 158.7 mA h g^{-1} at 200 mA g^{-1}, a capacity fading of only 0.0138% per cycle at 1 A g^{-1} for 1000 cycles, as well as high rate capability.

In the search of better electrode materials for SIBs, researchers believe that cooperative effect of binary metals, such as combination of Ni, Fe, Mn and Co, could be beneficial. However, earlier attempts were not very successful. For examples, $Na_2Ni_2TeO_6$ [45] and $NaNi_{0.5}TiO_2$ [46] were found to display continuous capacity decay upon cycling. Recently, honeycomb-ordered O3-phase $Na_3Ni_2SbO_6$ cathode cycling within the voltage range of 4.0–2.0 V exhibited a capacity retention of 94% after 50 cycles at 0.1 C, and remained 70% of the reversible capacity over 500 cycles at 2 C (400 mA g^{-1}) [47]. The reversible three-phase transformations (O3-$Na_3Ni_2SbO_6$ ↔ P3-$Na_2Ni_2SbO_6$ ↔ O1-$NaNi_2SbO_6$) may contribute to the good cyclability of the layered $Na_3Ni_2SbO_6$, which is evidenced by *ex-situ* X-ray diffraction (XRD) tests.

Another common approach is the partial substitution of other transition metals, especially Ti, in $Na_XT_MO_2$ cathodes. The electrochemical properties of P2-phase $Na_xMn_{1-y-z}Fe_yNi_zO_2$ was improved by substituting Mn with a small amount of Ti, owing to the suppression of Jahn–Teller distortion [48]. The aim is to increase the lattice space meanwhile maintain the lattice structure. The results show that the Na/Na[$Ni_{0.4}Fe_{0.2}Mn_{0.2}Ti_{0.2}$]$O_2$ batteries deliver a reversible capacity of 145 mA h g^{-1} with long-term cycling performance. In addition, Hu et al. designed a new tunnel-type $Na_{0.61}[Mn_{0.27}Fe_{0.34}Ti_{0.39}]O_2$ through partially or fully substitute the redox couple of the negative electrodes [49]. This unique structure renders its high stability in air or even in water. This cathode exhibits a usable capacity of 90 mA h g^{-1} with a high average voltage of 3.56 V (Fe^{3+}/Fe^{4+} redox couple). The full cell using hard carbon as the negative electrode can deliver a high voltage of 3.32 V with a reversible capacity of 300 mA h g^{-1} at a current rate of C/10.

Originating from the Ni^{4+}/Ni^{2+} redox reaction, a layered cathode material $NaNi_{1/3}Mn_{1/3}Co_{1/3}O_2$ cathode delivers a capacity of 120 mA h g^{-1} between 2.0 and 3.75 V, indicating a reversible insertion of 0.5 equivalent amount of sodium ions [50]. The cathode undergoes sequence O3→O1→P3→P1 phase transition during cycling, evidenced by *in-situ* XRD analysis. Electrochemically inactive element doping may further improve the electrochemical performance of electrode materials containing Na, Ni, Mn and Co, For example, Al-substituted $NaNi_{1/3}Mn_{1/3}Co_{1/3}O_2$ ($Na_{0.67}[Mn_{0.65}Ni_{0.15}Co_{0.15}Al_{0.05}]O_2$) cathode exhibits a high reversible capacity of 141 mA h g^{-1} at a current of 20 mA g^{-1}, maintaining a capacity of 125 mA h g^{-1} after 50 cycles [51]. Li-substituted sodium layered transition metal oxide fiber cathodes exhibit better electrochemical performance than Li-free fibers because partial Li substitution is helpful to stabilize the structure of the electrode material and hence enhance the electrochemical performance [52]. Among Li-substituted sodium layered transition metal oxide fibers in this report, $Na_{0.8}Li_{0.4}Ni_{0.15}Mn_{0.55}Co_{0.1}O_2$ can deliver the highest discharge capacity of 138 mA h g^{-1} at 15 mA g^{-1}.

In order to develop cathode materials with high capacity, good retention and rate capability for rechargeable SIBs, a radially-aligned hierarchical-formed columnar $Na[Ni_{0.6}Co_{0.05}Mn_{0.35}]O_2$ is presented [53]. The chemical compositions of the cathode material vary from the inner core ($Na[Ni_{0.75}Co_{0.02}Mn_{0.23}]O_2$) to the outer layer ($Na[Ni_{0.58}Co_{0.06}Mn_{0.36}]O_2$) in a single spherical particle, enables Ni-based redox reactions that bring high-capacity and high cycle performance. The unique structure is beneficial to the Na-ion diffusion rate along with the direction of nanorod. And the energy capacity is increased from the high tap density of spherical morphology and the inner high Ni composition. Meanwhile, the thermal stability and cycle retention is also increased through the outer high Mn composition. The discharge capacity of 157 mA h g^{-1} (15 mA g^{-1}) with a capacity of 125.7 mA h g^{-1} after

100 cycles is achieved by radially aligned hierarchical columnar structure $Na[Ni_{0.6}Co_{0.05}Mn_{0.35}]O_2$/Na half cells. The full cells deliver a reversible capacity of 143 mA h g^{-1} and a rate capability of 132.6 mA h g^{-1} at 1500 mA g^{-1} (10 C), which is attributed to the $Ni^{2+/3+/4+}$ electrochemical redox reaction. In addition, the cathode also exhibit good thermal stability even at −20 °C.

2.1.2. Prussian blue analogues

Prussian blue analogues (PBAs), which possess an open-framework crystal structure, have been closely investigated due to their special structure and interesting electrochemical and magnetic properties [54,55]. The open framework of the cubic lattice which contains ⟨100⟩ channels (~3.2 Å in diameter) and interstitial sites (~4.6 Å in diameter) [56], enables rapid solid-state diffusion of various ions, such as Li^+, Na^+, K^+, alkaline divalent ions and zeolitic water [57,58]. The electrochemical properties of PBAs can be ascribed to the redox behavior of the transition metal ions in PBAs. PBAs have been reported as electrode materials with good cycle life and rate performance in both aqueous and organic electrolytes for SIBs [59,60]. Recently, Cui et al. have demonstrated sodium manganese hexacyanomanganate ($Na_2Mn^{II}[Mn^{II}(CN)_6]$) without sodium vacancies (Fig. 3a) as a potential positive electrode for non-aqueous SIBs [61]. The open-framework structure enables high structural integrity while accommodating multiple sodium ions, thus leading to both fast kinetics and high capacity. The overall volume expansion is merely 1.36% during the range of electrochemical cycling, which reflects the stable crystal structure of open framework. The $Na_2Mn^{II}[Mn^{II}(CN)_6]$ exhibits a reversible capacity of 209 mA h g^{-1} in a propylene carbonate electrolyte at an average voltage of 2.65 V *vs.* Na/Na^+. The high discharge capacity has been achieved mostly due to the existence of three Na^+ insertion stages. In the most discharged state, the stronger interaction between Na^+ and $[Mn(CN)_6]^{5-}$ drives further displacement of Na^+, which creates sufficient space for two sodium ions.

Goodenough et al. has investigated the Na-enriched iron manganese hexacyano-perovskites in a non-aqueous electrolyte [55]. Rhombohedral $Na_{1.72}MnFe(CN)_6$ delivers a reversible capacity of 134 mA h g^{-1} between 2.0 and 4.2 V with good retention (~90% after 30 cycles). It delivers a capacity of 45 mA h g^{-1} at 40 C (Fig. 3b).

$Na_{0.61}Fe[Fe(CN)_6]_{0.94}$ and $FeFe(CN)_6$ exhibit high rate capability and cycle performance, but the low first-cycle Coulombic efficiency needs to be improved. Huang's group demonstrated the detailed relationship between coordination environment of Na^+ and Coulombic efficiency by experimental analysis and first-principle calculations [62]. They found that Na-rich $Na_{1.70}FeFe(CN)_6$ could deliver a capacity of 120.7 mA h g^{-1} at 200 mA g^{-1} and a capacity of 73.6 mA h g^{-1} even at 1200 mA g^{-1}. The results show that the first-cycle Coulombic efficiency of nanocubic $Na_xFeFe(CN)_6$ can be improved by adjusting the amount of sodium pre-storage.

2.1.3. Phosphates, fluorophosphates and pyrophosphates

Olivine $NaFePO_4$ has more thermodynamically stable maricite structure than olivine-type $LiFePO_4$, which has no free pathways for the diffusion of Na^+ [63]. Electrochemically active olivine-type $NaFePO_4$ as a cathode synthesized by low-temperature $Li^+ - Na^+$ exchange from $LiFePO_4$, has a theoretical capacity of 154 mA h g^{-1} and an operating potential of 2.9 V *vs.* Na/Na^+ [64]. However, olivine $NaFePO_4$ exhibit lower capacity than the theoretical capacity because of large volume change between the reduced and oxidized phases [65]. Maricite $NaFePO_4$ with the diameter of 50 nm exhibits reversible capacity of 142 mA h g^{-1} (1.5–4.5 V) and a capacity retention of 95% was offered after 200 cycles [66]. Na^+ can be deintercalated from the nano-sized maricite $NaFePO_4$ with simultaneous transformation into amorphous $FePO_4$, which is the key step for reversible Na^+ de/intercalation in the electrode. The amorphous $FePO_4$ can significantly enhance Na^+ mobility because only one fourth of the hopping activation energy barrier is needed in amorphous $FePO_4$. Tong et al. reported hollow amorphous $NaFePO_4$ nanospheres using a facile *in-situ* hard-template method [67]. The small size and relatively thin wall of the nanospheres give rise to the enhanced electrochemical performance, showing an initial capacity of 152 mA h g^{-1} at 0.1 C (1.5–4.0 V) and a capacity of 67.4 mA h g^{-1} at 10 C. The authors also predicted that amorphous $NaFePO_4$ might have more opportunities for SIBs than the olivine and maricite phases.

$Na_3V_2(PO_4)_3$, as a sodium super ionic conductor (NASICON) with large tunnels for the fast conduction of Na^+, has been regarded as a promising cathode material for SIBs due to its high theoretical energy density of 400 Wh kg^{-1} (117.6 mA h g^{-1} × 3.4 V for V^{3+}/V^{4+}) and thermal stability during charge process [68]. Fig. 4 shows the NASICON framework of $Na_3V_2(PO_4)_3$. The open and 3D characteristics of the NASICON framework are beneficial for facile Na^+ migration. The electrochemical profile of $Na_3V_2(PO_4)_3$ show a voltage plateaus at 3.4 V, which corresponds to the reversible V^{3+}/V^{4+} redox reaction. Recent reports have demonstrated the improvement of its cycling stability and rate capability by utilizing carbon supporting [69], coating [70] or embedding [71] approaches. For example, the $Na_3V_2(PO_4)_3$ coated by 6 wt% carbon displays a reversible capacity of 114 mA h g^{-1} at 1 C and a capacity retention of 50% after 30000 cycles at 40 C [68]. Nanosized $Na_3V_2(PO_4)_3$ embedding into porous carbon can deliver a specific capacity of 44 mA h g^{-1} at 22 A g^{-1} (200 C), corresponding to charging-discharging in only 6 s [69]. Additionally, hierarchical carbon framework is very effective to enhance the transport of electrons and Na^+, and to accommodate the volume variation during Na^+ insertion/extraction. Yang et al. prepared hierarchical carbon framework wrapped $Na_3V_2(PO_4)_3$ by chemical vapor deposition, which consists of graphene-like carbon layers and interconnected nanofibers [72]. This cathode material exhibits an ultra-high rate capacity of 78 mA h g^{-1} at 100 C and a capacity retention of 54% after 20000 cycles at 30 C.

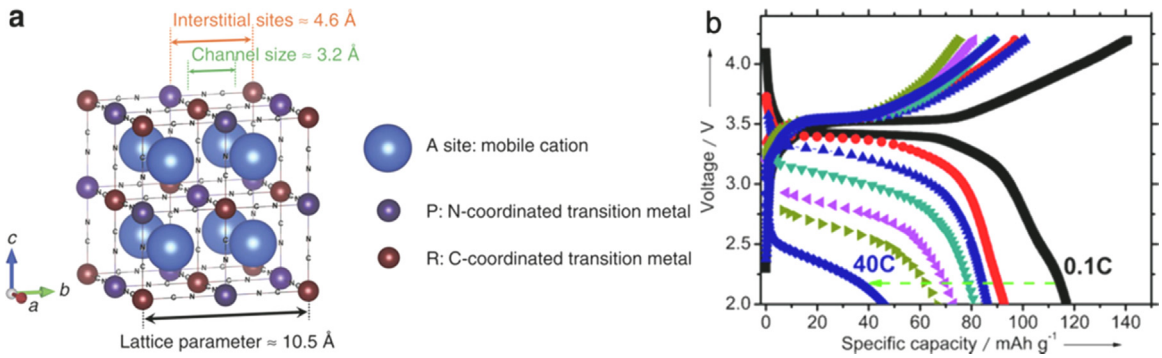

Fig. 3. (a) Crystal structure of open-framework $Na_2Mn[Mn(CN)_6]$ [61]. (b) Electrochemical performance of $Na_xMnFe(CN)_6$ cathode [55].

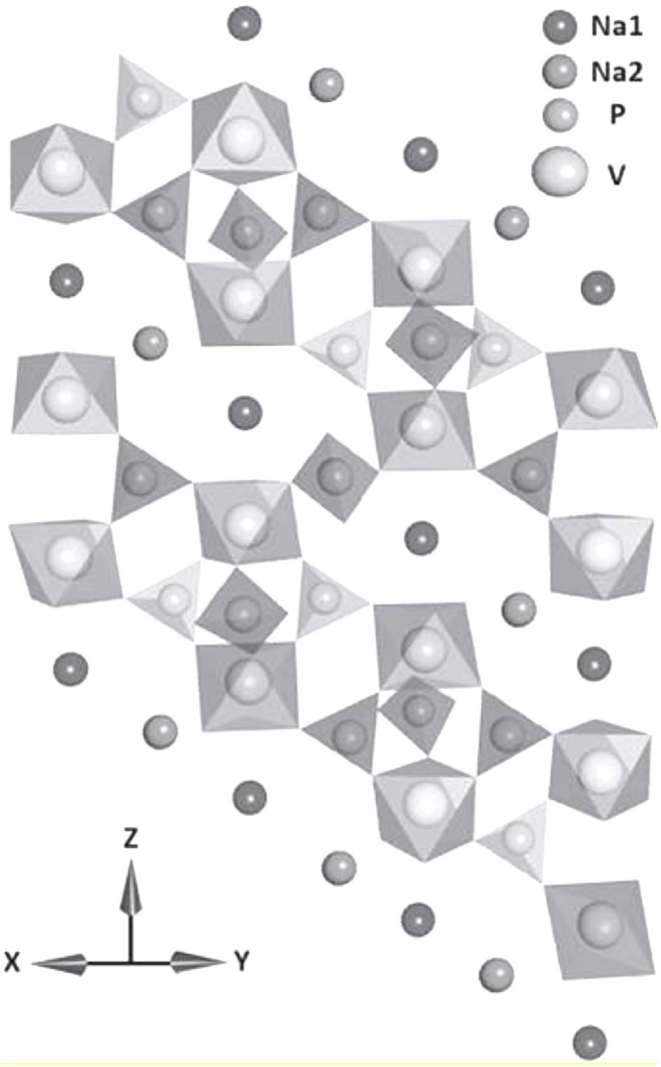

Fig. 4. The crystal structure of the $Na_3V_2(PO_4)_3$ NASICON structure on the *ab* plane [68].

The electrochemical performance of $Na_3V(PO_4)_3$ with a NASICON-type framework can be further enhanced by the substitution of electronegative fluorine atoms. One example is $Na_3V_2(PO_4)F_3$ consisting of $V_2O_8F_3$ bi-octahedra and PO_4 tetrahedron units [73]. It displays two voltage plateaus occurring at 3.7 V and 4.2 V, respectively, assigning to a two-step V^{4+}/V^{3+} redox reaction [74]. Additionally, $Na_3(VO_x)_2(PO_4)_2F_{3-2x}$ $(0 \le x \le 1)$ has been prepared by the substitution of fluorine to oxygen. Fig. 5 shows the crystal structure of $Na_{1.5}VPO_{4.8}F_{0.7}$, in which the corner-sharing between PO_4 tetrahedral units and VO_5F/VO_4F_2 octahedral units constructs a three-dimensional open framework, and Na^+ can be inserted into the interstitial sites forming Na layers on the *ab* plane in the structure [75]. For instance, $Na_3(VO_{0.8})_2(PO_4)_2F_{1.4}$ reported by Kang's group can deliver a reversible capacity of 155.6 mA h g^{-1} (specific energy of ~600 W h g^{-1}) with 95% and 84% capacity retention for 100 and 500 cycles at 60 °C, respectively. Such an outstanding cycle life derives benefit from the small volume expansion (2.9%) during cycling.

Inspired by the success of $Li_2MP_2O_7$, Yamada research group has developed a series of sodium analogues with smooth Na^+ mobility as candidate cathode materials, such as orthorhombic $Na_2CoP_2O_7$, triclinic $Na_2FeP_2O_7$ and $Na_2MnP_2O_7$ [76]. The $Na_2MP_2O_7$ materials can achieve a reversible capacity of 80–90 mA h g^{-1} with an average voltage of ~3.0 V for $Na_2FeP_2O_7$ [77] and $Na_2CoP_2O_7$ [78] and ~3.7 V for orthorhombic $Na_2MnP_2O_7$ [79]. Besides, the mixed phosphate/pyrophosphate compounds ($Na_4Co_3(PO_4)_2P_2O_7$ and $Na_4Fe_3(PO_4)_2P_2O_7$) also have been investigated as cathode materials for SIBs [80,81]. The representative $Na_4Co_3(PO_4)_2P_2O_7$ offers a reversible capacity of 95 mA h g^{-1} at 34 mA g^{-1} with a high voltage of 4.4 V, without observable fading after 100 cycles [80].

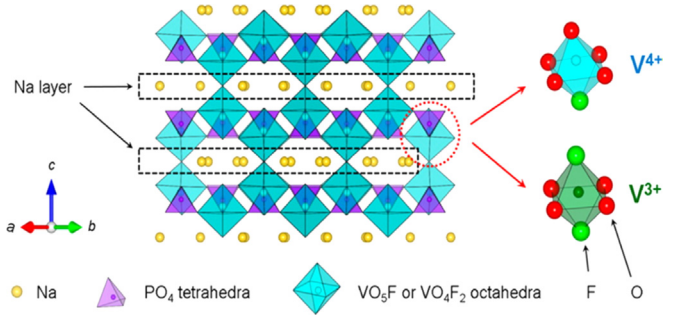

Fig. 5. Crystalline lattice structure of $Na_{1.5}VPO_{4.8}F_{0.7}$ and two different local bonding states for V^{4+} and V^{3+} ions (VO_5F and VO_4F_2 octahedra, respectively) [75].

2.1.4. Sulfates

Sulfates have been considered as cathode candidates for SIBs more recently. Bloedite-type $Na_2M(SO_4)\cdot 4H_2O$ (M=Mg, Fe, Co or Ni) and their dehydrated derivatives $Na_2M(SO_4)_2$ (M=Co or Fe) show electrochemical activity at potential 3.3–3.4 V *vs.* Na/Na^+. However, the reversible capacity of $Na_2Fe(SO_4)$ and $Na_2Fe(SO_4)\cdot 4H_2O$ are normally lower than 100 mA h g^{-1} [82]. Yamada et al. reported Kröhnkite-type $Na_2Fe(SO_4)_2\cdot 2H_2O$ [83] and alluaudite-type sulfate framework $Na_2Fe_2(SO_4)_3$ [84] with the Fe^{3+}/Fe^{2+} redox potential at 3.25 V and 3.8 V *vs.* Na/Na^+, respectively. Fig. 6 shows the crystal structure of $Na_2Fe_2(SO_4)_3$. The advantage to use $(SO_4)^{2-}$ instead of $(PO_4)^{3-}$ is to stabilize the $Na_2Fe_2(SO_4)_3$ compound, which only contains Fe^{2+} (no Fe^{3+}) and partially occupied Na^+ sites suitable for fast Na^+ diffusion upon electrode reaction. Moreover, $Na_2Fe_2(SO_4)_3$ delivers a reversible capacity of 102 mA h g^{-1} and high-rate capability due to a very small volume change of 1.6% upon sodiation/desodiation.

In this section, we have reviewed many different positive electrode materials for SIBs. Among them, polyanionic-framework materials that have available octahedral interstitials in lattices and layered oxide materials that have two-dimensional galleries for holding Na^+ in 6-coordinate geometry should be the two most promising classes of cathode materials. The increased size of Na^+ suggests that Na^+ diffusion in similarly-structured host materials would be slower compared to Li^+, implying power restriction in SIBs. Although the cathode research in SIBs is somewhat fruitful, more progress is still required to realize the practical deployment of SIBs.

2.2. Anode materials

The metallic sodium has high reactivity with conventional organic electrolytes and has the tendency to form dendrites during Na deposition if directly used as anode. Hence, instead of reactive Na metal, it is critical to look for other anode materials in which Na^+ can be cycled back and forth in a 'rocking-chair' format [18]. Unfortunately, the anode part of SIBs is one of the most troublesome components because typical graphitic carbons used in LIBs are incapable of intercalating Na^+ [85]. Up to date, only a few of anode materials with adequate capacity and fair cyclability for SIBs have been developed. The anode materials reported in the literature are listed in Table 3 and discussed as below.

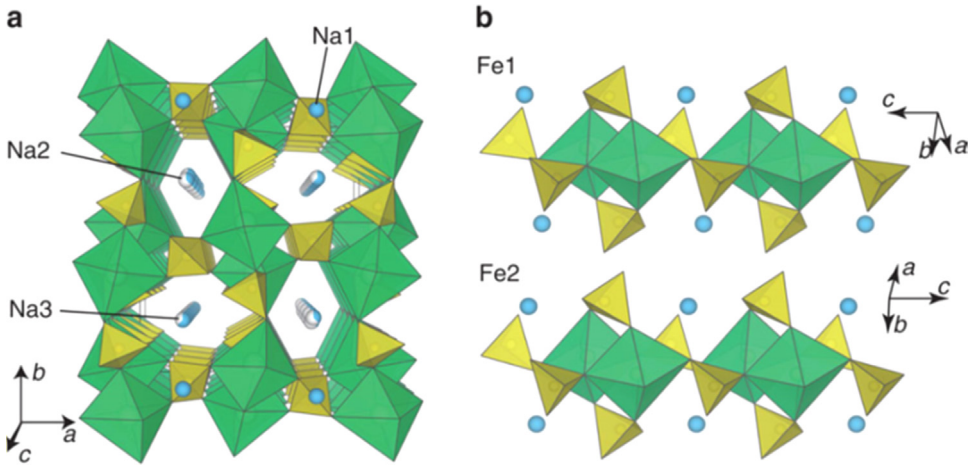

Fig. 6. View of the phase structure of $Na_2Fe_2(SO_4)_3$ [84].

2.2.1. Carbon-based materials

For anode materials in SIBs, various carbon materials with different structures (such as soft carbons, hard carbons, amorphous carbon, hydrogen-contained carbons and reduced graphene oxides) [86,87] and different morphologies (such as carbon nanowires and hollow carbon nanospheres) [88,89] have been investigated, normally delivering a reversible capacity of about 250–300 mA h g^{-1} at very low current density (below 50 mA g^{-1} at a voltage range from 0 to 3 V). However, it is difficult to further enhance their capacity due to the limited sodium host sites in carbon structures.

Most of the carbon-based anodes consist of few-layer-stacked graphitic nanocrystallites with interlayer distances in the range of 0.37–0.40 nm [88]. The studies of carbon-based anodes are focused on hard carbons because they have large interlayer distance and disordered structure, which facilitates sodiation/desodiation [89,90]. Dahn et al. have reported that hard carbon originated from pyrolyzed glucose presents an initial reversible capacity as high as 300 mA h g^{-1} and a significant portion of their capacity locates at a potential close to that of Na metal since the discharge cutoff voltage is below 0 V [90]. As the authors suggested, the sodium storage mechanism in disordered carbon can be considered similar to that of lithium. Similarly, hollow carbon nanowires prepared by pyrolysis of hollow polyaniline nanowires deliver a reversible capacity of 251 mA h g^{-1} and 82.2% capacity retention over 400 cycles [88]. The short diffusion distance in the hollow carbon nanowires and the large interlayer distance of 0.37 nm between graphitic sheets contribute to the good performance. Fig. 7 shows the equilibrium interplanar distance of NaC_6 (0.45 nm) and LiC_6 (0.37 nm). When the layer spacings between graphite layers (0.335 nm) increase to 0.37 nm, the energy barrier for Na^+ insertion drops remarkably from 0.12 eV to 0.053 eV. This energy barrier is low enough to overcome. Operating hard carbon anodes in SIBs at high current density and/or high depth of discharge easily leads to safety issue, since the potential of Na^+ insertion in hard carbons is very close to the deposition potential of sodium. A porous hard carbon prepared based on a silica template method reported by Adelhelm et al. shows a possible solution [91]. The hierarchical porosity greatly enhanced rate capability at room temperature. Recently, several reports have shown that hard carbons with relatively low specific surface area exhibit a high initial Coulombic efficiency and good cyclic stability [92–94]. The high specific surface area could induce the formation of solid-electrolyte interface (SEI) layer making these carbons out of function, while low specific surface area could leave enough interlayer space for Na^+ intercalation [95]. A commercial carbon molecular sieve demonstrates good Na^+ storage performance of 284 mA h g^{-1} after 180 cycles at a current density 100 mA g^{-1} with high initial Coulombic efficiency of 73.2%. The good performance is derived from the low specific surface area of 17 m^2 g^{-1} and its abundant ultra-small pores (0.3–0.5 nm) that allow the insertion of Na^+ while rejecting the electrolyte [96].

Graphite is an intriguing material with high lithium storage capacity (~372 mA h g^{-1} in LIBs), but its sodium storage capacity is very low (less than 35 mA h g^{-1} in SIBs) [97]. As depicted by recent theoretical calculations, a minimum interlayer distance of 0.37 nm is believed to be required for Na^+ insertion, while the interlayer distance of graphite (~0.34 nm) is too small to accommodate Na^+ [88]. Interestingly, Wang et al. prepared expanded graphite with an enlarged interlayer lattice distance of 4.3 Å, but maintaining a long-range-ordered layered structure [85]. The interlayer spacing of expanded graphite can be manipulated by controlled oxidation and reduction processing, and it has a strong influence on the reversible capacity. Fig. 8 shows the cross-sectional views of pristine graphite, graphite oxide, expanded graphite-1 h and expanded graphite-5 h. The average interlayer spacings were measured to be 0.34, 0.61, 0.43 and 0.37 nm, respectively. And the discharge capacity of the samples are 13, 156, 300, 100 mA h g^{-1} at 20 mA g^{-1}, in sequence. The reversible capacity increases from 25 mA h g^{-1} in graphite (d=3.4 Å) to 100 mA h g^{-1} in highly-reduced graphene oxide (d=3.7 Å), and reaches 280 mA h g^{-1} at the optimal interlayer spacing of 4.3 Å. The optimized expanded graphite shows a stable reversible capacity of about 280 mA h g^{-1} at current density of 20 mA g^{-1}, presents a capacity of 184 mA h g^{-1} at 100 mA g^{-1} with 73.92% capacity retention after 2000 cycles (Fig. 9).

The further commercialization of carbonaceous materials for SIBs is limited by the high cost and the low initial Coulombic efficiency. Recently, an amorphous carbon material was fabricated through direct pyrolysis of low-cost pitch and phenolic resin, displaying high initial Coulombic efficiency of 88% in SIBs with a high reversible capacity of 284 mA h g^{-1} and good cycling performance [98]. The full cell shows an initial Coulombic efficiency of 80%, a good cycling stability and an energy density of 195 W h kg^{-1} based on the total mass of electrode materials when coupled with an air-stable O_3-$Na_{0.9}[Cu_{0.22}Fe_{0.30}Mn_{0.48}]O_2$ cathode.

2.2.2. Phosphorus and phosphides

Phosphorus is a particularly attractive anode material for SIBs, which can form sodium phosphide (Na_3P) upon the complete reaction of with Na. This three-electron-transfer reaction provides the highest theoretical capacity of 2595 mA h g^{-1} among known anode materials for SIBs and a relatively safe working potential

Table 3
Electrochemical properties of typical anode materials for SIBs reported in the literature.

Electrode material	Ref.	Reversible capacity (mA h g^{-1})	Current density (mA g^{-1} or C)	Capacity retention
1. Carbon-based materials				
Reduced grapheme oxide	[87]	174.3	40	81% after 1000 cycles at 0.2 C
Hollow carbon nanowires	[88]	251	50	82.2% after 400 cycles at 50 mA g^{-1}
Hollow carbon nanospheres	[89]	223	50	71% after 100 cycles at 50 mA g^{-1}
Hollow carbon nanospheres	[91]	> 180	C/5	44% after 125 cycles at C/5
Ternary graphite intercalation compounds	[92]	~100	0.1 C	–
3D folded-graphene	[93]	120 mA h cm^{-3}	0.1 A g^{-1}	84% after 1600 cycles at 0.5 A g^{-1}
Hard carbon microspheres	[94]	322	C/10	–
Natural graphite (ether-based electrolyte)	[95]	127	500	80% after 2500 cycles at 100 mA g^{-1}
Carbon molecular sieve	[96]	300	100	93.3% after 180 cycles at 100 mA g^{-1}
Expanded graphite	[85]	284	20	73.92% after 2000 cycles at 100 mA g^{-1}
Amorphous carbon	[98]	284	0.1 C	94% after 100 cycles at 0.2 C
2. Phosphorus and phosphides				
C-amorphous phosphorus	[99]	1800	250	66.7% after 80 cycles at 1 A g^{-1}
Amorphous red phosphorus/carbon	[100]	1890	143	80% after 30 cycles at 143 mA g^{-1}
Phosphorus/graphene nanosheets	[101]	2077	260	95% after 60 cycles at 260 mA g^{-1}
Red P/single-walled carbon nanotubes	[102]	700	50	80% after 2000 cycles at 2 A g^{-1}
Commercial red P/carbon nanotubes	[103]	1675	143	76.6% after 10 cycles at 143 mA g^{-1}
FeP	[104]	764.7	50	69% after 60 cycles at 50 mA g^{-1}
NiP_3	[105]	966	0.1 C	89% after 15 cycles at 0.1 C
SnP_3/C	[106]	810	150	92% after 150 cycles at 150 mA g^{-1}
Sn_4P_3	[107]	850	100	86% after 150 cycles at 100 mA g^{-1}
Sn_4P_3	[108]	718	100	–
3. Metal alloys				
Porous carbon/tin	[109]	359	20	–
Sn50Ge25Sb25	[110]	833	425	90% after 50 cycles at 425 mA g^{-1}
Sb	[112]	600	1 C	80% after 100 cycles at 20 C
Ni–Sb	[113]	632	1 C	63% after 150 cycles at 1 C
Sn@carbon nanotube-carbon paper	[114]	887 mA h cm^{-2}	50 mA cm^{-2}	62% after 100 cycles at 50 mA cm^{-2}
$Bi_{0.57}Sb_{0.43}$-C	[115]	375	100	76 after 50 cycles at 100 mA g^{-1}
SnSb/C	[116]	544	100	80% after 50 cycles at 100 mA g^{-1}
Sn/C	[117]	493	1000	84% after 500 cycles at 1000 mA g^{-1}
Sb/C	[35]	631	C/15	90% after 400 cycles 200 mA g^{-1}
4. Metal oxides				
$Na_2Ti_3O_7$	[118]	180	C/25	–
$NaTiO_2$	[119]	152	C/10	98% after 60 cycles at C/10
$Na_{0.66}Li_{0.22}Ti_{0.78}O_2$	[120]	116	C/10	75% after 1200 cycles at 2 C
$NaTi_2(PO_4)_3$	[121]	123	0.2 mA cm^{-2}	–
$Na_{0.44}[Mn_{0.44}Ti_{0.56}]O_2$	[122]	100–110	C/10	> 96% after 1100 cycles at 1 C
γ-Fe_2O_3@C	[123]	993	200	75% after 200 at 200 mA g^{-1}
Porous CuO arrays	[124]	935	20	45.2% after 450 at 200 mA g^{-1}
α-MoO_3	[126]	410	0.1 C	55% after 500 cycles at 0.2 C
Al_2O_3 coating-MoO_{3-x}	[127]	385.1	200	–
5. Metal chalcogenides				
FeS_2	[128]	170	20	90% after 20000 cycles at 1 A g^{-1}
MoS_2/carbon	[129]	671	0.1 C	~100% after 300 cycles at 1 C
FeS_2	[131]	800	1000	50% after 300 cycles at 1 A g^{-1}
Micro-MoS_2	[132]	420	50	83% after 70 cycles at 1 A g^{-1}
MoS_2 nanoflowers	[133]	350	50	~100% after 1500 cycles at 10 A g^{-1}
$MoSe_2$	[134]	527	200	after 50 cycles at 200 mA g^{-1}
$FeSe_2$ microspheres	[135]	447	100	89% after 2000 cycles at 1 A g^{-1}

(~0.45 V *vs.* Na/Na^+) [99,100]. However, the application of red phosphorus in SIBs is impeded by its poor electrical conductivity (~10^{-14} S cm^{-1}), low diffusivity, and large volume change (~300%) leading to the cracks in anodes and loss of electrical contacts during sodiation/desodiation. To solve these problems, red phosphorus was often mixed with carbon (such as graphene or carbon nanotubes) to form red phosphorus/carbon composites by high-energy ball milling process or vaporization-condensation method [101–103]. Additive carbon components are able to enhance the conductivity of the phosphorus/carbon composites and accommodate the volume change of phosphorus during sodiation/desodiation cycles, hence beneficial to the electrochemical performance [100]. Wang et al. developed a red phosphorus/single-walled carbon nanotube composite by using a modified vaporization-condensation method [102]. Carbon nanotubes and red phosphorus are uniformly mixed with each other in the composite, and very limited amount of phosphorus is inside the single-walled carbon nanotube bundles, which ensures a high electronic conductivity for the composite. The composite displays a high discharge capacity (~700 mA h g^{-1} at 50 mA g^{-1}), fast rate capability (~300 mA h g^{-1} at 2000 mA g^{-1}), and good cycling life with 80% capacity retention after 2000 cycles.

Phosphides (FeP_x, NiP_x) also have been introduced as anodes for SIBs [104,105]. The metal element (Fe) in FeP are supposed to be inactive and only act as a conductive matrix to buffer the volume variation [104]. Comparatively, NiP_3 showed a reversible storage capacity of 900 mA h g^{-1} after 15 cycles [105]. The capacity fading was attributed to the continuous formation of SEI layer on the surface newly exposed to electrolyte because of the volume change during cycling. The reversible reaction during discharge is

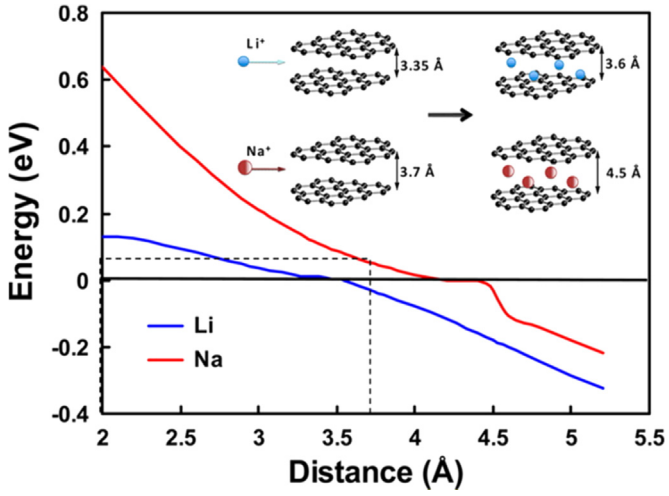

Fig. 7. Theoretical energy cost for Na^+ and Li^+ insertion into carbon as a function of the interlayer distance of carbon [88]. The inset shows the mechanism of Na^+ and Li^+ insertion into carbon.

proposed as follows:

$$NiP_3 + 9Na^+ + 9e^- \rightarrow 3Na_3P + Ni \quad (1)$$

In addition, Wang et al. reported SnP_3-based anode material for the SIBs [106]. The SnP_3/C composites synthesized by ball-milling deliver a high capacity of 810 mA h g^{-1} at current density of 150 mA g^{-1} over 150 cycles without noticeable capacity decay. The SnP_3/C anodes shows matched cycling stability and higher capacity compared to reported Sn_4P_3 (460–718 mA h g^{-1}) at similar current [107]. As illustrated in Fig. 10, Sn and P components in the Sn_4P_3/C material are combined to give a synergistic Na-storage mechanism. The Sn atoms form electronic channels to activate the sodiation reaction of P atoms, while the resulting Na_3P phase forms a protective matrix to avoid the aggregation of the Sn particles, thus generating a stable electrochemical environment in the anode. The reversible reaction mechanism of SnP_3 during discharge is similar to Sn_4P_3 [108]:

$$SnP_3 + 9Na^+ + 9e^- \rightarrow Sn + 3Na_3P \quad (2)$$

$$4Sn + 15Na^+ + 15e^- \rightarrow Na_{15}Sn_4 \quad (3)$$

2.2.3. Metal alloys

Alloy-based anodes, such as Sn ($Na_{15}Sn_4$, 847 mA h g^{-1}) and Sb (Na_3Sb, 660 mA h g^{-1}), have attracted considerable interest due to their appropriate potential of Na^+ insertion and high theoretical capacities for SIBs [35,109]. Many alloy-based anodes consisted of one or more different metals (e.g., Sn, Sb, Ge, Ni, SnSb or SnSbGe) have been investigated [110–113]. Among them, Sn is a promising candidate with an average voltage of 0.3 V (*vs.* Na/Na^+) and a theoretical capacity of 790 mA h g^{-1}. However, the large volume change of alloys severely hinders their practical applications. For example, 520% of volume expansion (from Sn to $Na_{15}Sn_4$) would suppress the achievement of high capacity [106,114]. Attempts have been made to reduce the volume change [109,115,116]. Chen et al. prepared ultrasmall (~8 nm) Sn nanoparticles homogeneously embedded in spherical carbon network [117]. The high porosity and high electrical conductivity of the Sn/C framework would promote the reversible sodiation/desodiation, which is favorable for high-rate capability. Moreover, the size of Sn nanoparticles has a great effect on rate capability and cycling performance (Fig. 11).

Antimony (Sb) has been demonstrated to display high cycling stability [116]. Cao et al. synthesized Sb/C nanofibers delivering large reversible capacity of 631 mA h g^{-1} at C/15, improved rate capability of 337 mA h g^{-1} at 5 C and long-term cyclability with 90% capacity retention after 400 cycles [35]. The superior performance and stability was attributed to the unique structure of metal/carbon composite nanofibers with uniform distribution of Sb nanoparticles implanted in carbon matrix.

2.2.4. Metal oxides

Titanates usually exhibit good stability at low voltage. $Na_2Ti_3O_7$ consists of zigzag layers of titanium-oxygen octahedra with sodium ions in the interlayer spaces that can be easily exchanged, and it also exhibits a particularly low potential [118]. The insertion of two additional Na^+ (180 mA h g^{-1}) in the lattice and the reduction of two of three Ti(IV) species to Ti(III) occur at a reversible plateau around 0.3 V *vs.* Na/Na^+ at low cycling rate (C/25). Moreover, the rate capability can be further improved by the decrease of particle size. Ceder et al. reported layered $NaTiO_2$ as a

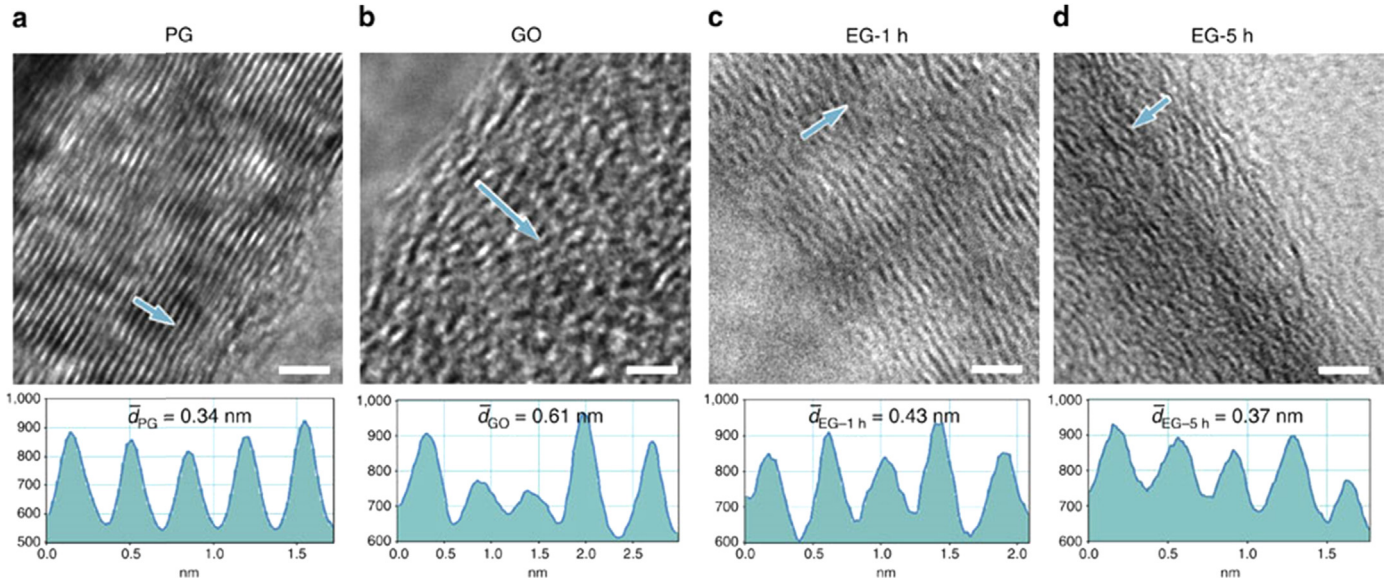

Fig. 8. The cross-sectional views of (a) pristine graphite, (b) graphite oxide, (c) expanded graphite-1 h and (d) expanded graphite-5 h characterized by high-resolution transmission electron microscopy. The scale bars are 2 nm. Contrast profiles along the arrows indicate the interlayer spacings of samples [85].

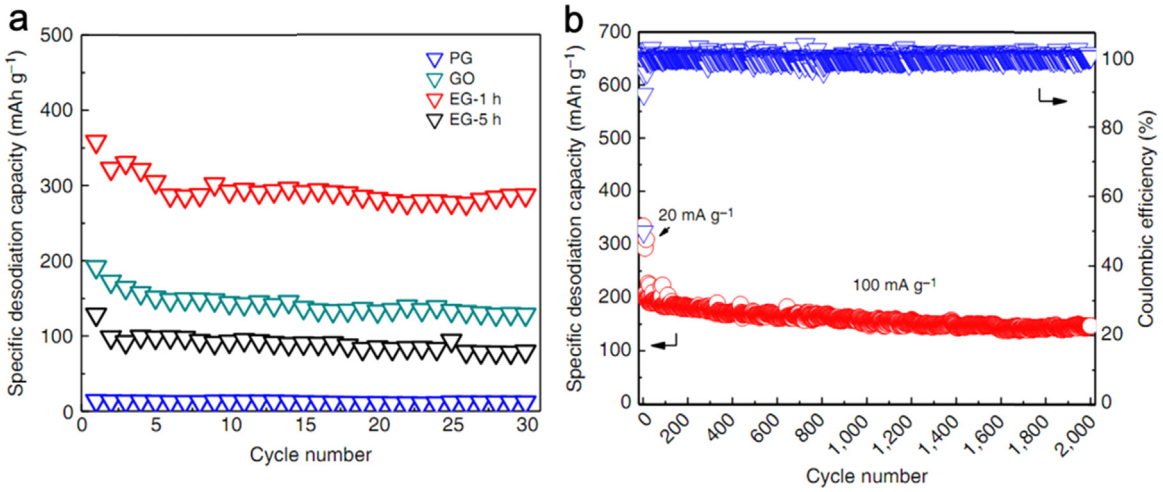

Fig. 9. (a) Short-term cycling stability tests of pristine graphite, graphene oxide and expanded graphite at 20 mA g^{-1}. (b) Long-term cycling stability of expanded graphite-1 h (20 mA g^{-1} was used for the initial 10 cycles) [85].

promising intercalation anode material for SIBs [119]. To achieve high capacity and cyclability, the optimal voltage window for galvanostatic cycling was located between 0.6–1.6 V. X-ray diffraction indicated that a reversible $O_3-O'_3$ phase transition occurred, including a lattice parameter variation along with complicated Na vacancy orderings, which yielded a constant interslab distance and slightly changing in-plane Ti–Ti distance in the O'_3 phase. Another layered material, $Na_{0.66}Li_{0.22}Ti_{0.78}O_2$, shows only ~0.77% volume change during sodiation/desodiation [120]. Fig. 12 displays the crystal structure of P2-type zero-strain layered $Na_{0.66}Li_{0.22}Ti_{0.78}O_2$. Different from O3-type material, the repulsive Coulomb interaction of the AA-type oxygen stacking brings a larger interlayer of ~5.56 Å. The P2-type layered material exhibits an unusual quasi-single-phase electrochemical storage behavior and long-term cyclic stability, which is contrast to other P2-type materials demonstrating several plateaus during sodium extraction/insertion related to multiple phase transition processes. The $Na_{0.66}Li_{0.22}Ti_{0.78}O_2$ anode shows a capacity retention of 75% after 1200 cycles in a half cell.

Okada et al. have reported that NASICON-type $NaTi_2(PO_4)_3$ anode in both non-aqueous and aqueous electrolytes presents a reversible capacity of 133 mA h g^{-1} (93% of the theoretical capacity) with a plateau voltage of 2.1 V *vs.* Na/Na^+ [121]. Compared to non-aqueous electrolyte, the polarization observed in the aqueous electrolyte was remarkably smaller due to its low impedance and viscosity. Meanwhile, the sodiation/desodiation potential is located at the lower limit of the electrochemical stability window of the aqueous Na_2SO_4 electrolyte. Ti-substituted $Na_{0.44}MnO_2$ ($Na_{0.44}[Mn_{1-x}Ti_x]O_2$) with tunnel structure can also be used as anode for aqueous SIBs, exhibiting superior cyclability even without special oxygen-removal treatment from the aqueous solution [122]. Fig. 13 shows *in-situ* XRD data of the electrode during Na^+ insertion and extraction. It was concluded that the phase transition proceeded through several solid-solution reactions during Na^+ insertion/extraction into/from $Na_{0.44}[Mn_{0.44}Ti_{0.56}]O_2$. The authors suggested that Ti substitution tuned the reaction pathway and charge ordering property, thus significantly lowering the voltage of Na^+ storage and smoothing the charge–discharge profiles.

Metal oxides (e.g., Fe_2O_3 and CuO) that undergo a conversion reaction with sodium often have high theoretical capacity, but their performances are usually hampered by poor cycling life due to large volume and structure change. Chen et al. reported a three-dimensional porous γ-Fe_2O_3@C nanocomposite comprising γ-Fe_2O_3 nanoparticles (~5 nm) embedded in a porous carbon matrix, maintaining a reversible capacity of 358 mA h g^{-1} at a high current density of 2000 mA g^{-1} after 1400 cycles [123]. Zhang et al. synthesized flexible and porous CuO nanorod arrays as binder-free electrodes, which offer abundant open space, short and fast electron transporting paths [124].

Defects such as oxygen vacancies in metal oxides are of particular interest because they can trigger changes in the electronic structure of materials, thus having a significant effect on electron and ion transport [125]. MoO_3 delivers comparative capacity as SIB anode at deep-discharge condition (< 0.1 V *vs.* Na/Na^+) [126]. Lei et al. demonstrate the effect of oxygen vacancies by using MoO_{3-x} nanosheets as anodes in SIBs, which exhibited improved electrochemical performance compared to the MoO_3 counterpart due to

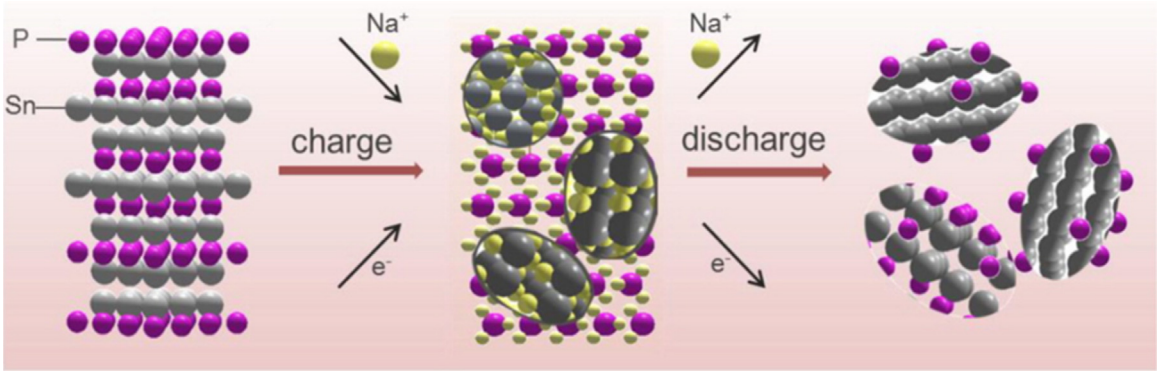

Fig. 10. Schematic diagram of the Na^+ storage mechanism in Sn_4P_3 electrode [107].

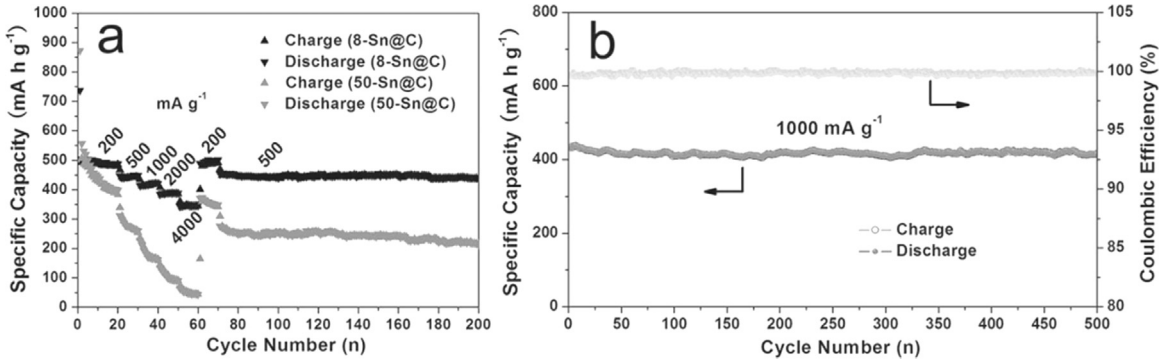

Fig. 11. (a) Rate capability and cycling performance of the Sn/C electrodes with different size of Sn nanoparticles (8 nm for 8-Sn@C and 50 nm for 50-Sn@C). (b) Cycle stability of the 8-Sn@C electrode at a 1000 mA g^{-1} [117].

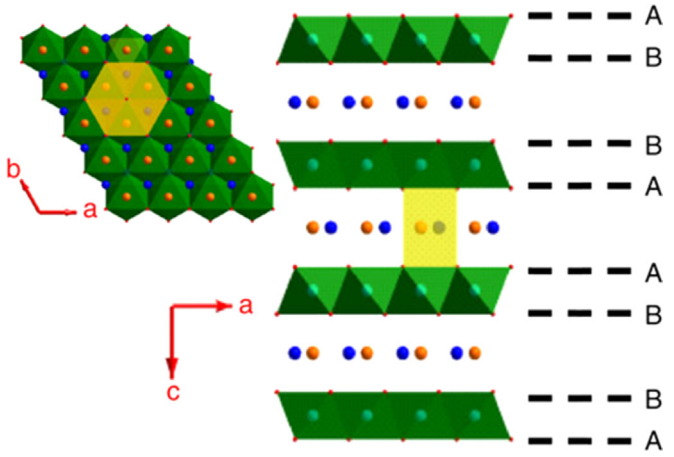

Fig. 12. Crystal structure of layered $Na_{0.66}Li_{0.22}Ti_{0.78}O_2$.

the enhanced electric conductivity and Na^+ diffusion coefficient [127]. Besides, the authors found Al_2O_3 coating can reduce the cycling-induced SEI formation, promoting the effect of oxygen vacancies at deep-discharge conditions.

2.2.5. *Metal chalcogenides*

Transition metal sulfides (including FeS_2, MoS_2, SnS_2 *etc.*) have been reported as anodes for SIBs [128,129]. Pyrite FeS_2 can be easily obtained from natural sources and possesses the advantages of being cheap and eco-friendly [130,131]. However, its application is hindered by the inferior cycling life in both LIBs and SIBs. By adopting diglyme as the electrolyte and adjusting the cut-off voltage to 0.8 V, the capacity of FeS_2 can reach 170 mA h g^{-1} at 20 A g^{-1} and the cell cycling at 1 A g^{-1} achieves high capacity retention of 90% after 20000 cycles [128]. The enhanced performance stems from two main points. First, a stable conductive layer-structured Na_xFeS_2 formed during cycling, which enables the highly reversible Na^+ intercalation/deintercalation. Second, the unprecedented high-rate characteristics were acquired because of the pseudocapacitance-type reactions. Two-dimensional layered materials, such as MoS_2 and SnS_2, have larger interlayer spacing and weak interlayer van der Waals force, allowing them to store Na^+ [132]. Chen et al. reported the synthesis of MoS_2 nanoflowers with expanded interlayers [133]. In particular, controlling the voltage range of 0.4–3.0 V preserves the layer structure through the intercalation reaction from MoS_2 to Na_xMoS_2, which delivers an increasing capacity with cycling because the expansion and exfoliation of MoS_2 layers produced more reaction sites and lower energy barrier for Na^+ intercalation/deintercalation.

Transition metal selenides, such as $MoSe_2$ and $FeSe_2$, also have been used as anode materials for SIBs [134,135]. Among them, $FeSe_2$ exhibits good electrochemical properties with a discharge capacity of 447 mA h g^{-1} at 0.1 A g^{-1} and good rate capability (388 mA h g^{-1} at 10 C, 226 mA h g^{-1} at 50 C, where 1 C=0.5 A g^{-1}) [135]. The remarkable high-rate performance is attributed to the pseudo-capacitive behavior during the charge–discharge processes based on a conversion mechanism.

In this section, recent research progresses on different classes of negative electrodes for SIBs are summarized. Most of the

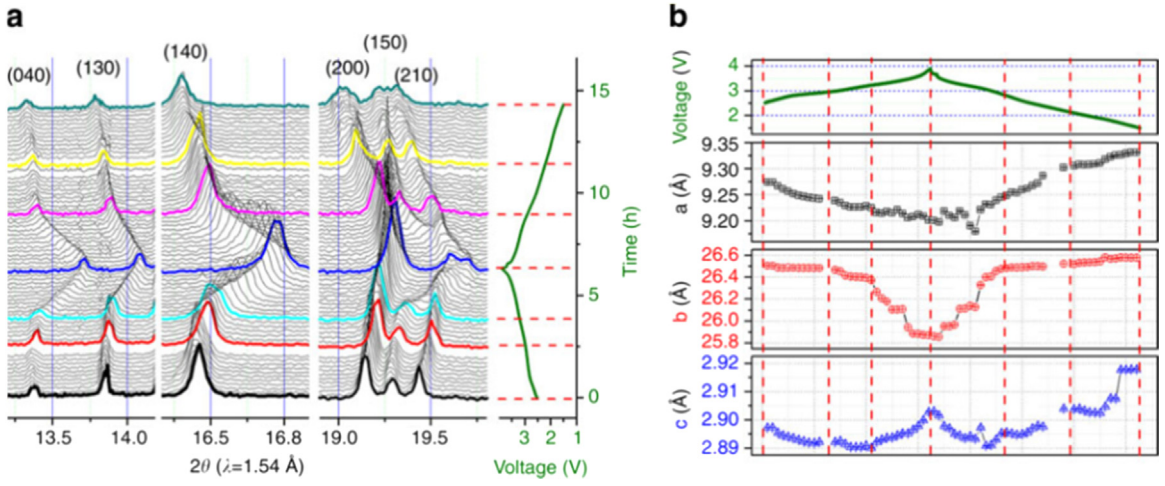

Fig. 13. Structure change upon Na^+ extraction/insertion [122]. (a) *In-situ* XRD patterns during the first discharge/charge cycle of the $Na/Na_{0.44}[Mn_{0.44}Ti_{0.56}]O_2$ cell at 0.1 C between 1.5–3.9 V. (b) Evolution of lattice parameters during charge/discharge process.

insertion-type and conversion-type anode materials show relatively low energy density. The energy density for hard carbons is ~300 mW h g^{-1} based on the mass of active material. The energy density for Sn and P based anodes reach 350 mW h g^{-1}, although P shows highest theoretical capacity of 2595 mA h g^{-1}. Currently, the anode is one of the most difficult components for SIBs because typical graphitic carbons used in LIBs cannot be intercalated by Na^+. Until now, only a few of anode materials have been demonstrated with decent capacity and acceptable cyclability. Compared to the Li equivalents, the voltage of SIBs is generally lower, the volume change upon Na^+ insertion/extraction is larger, the volumetric energy density is normally lower and the cycling stability is inferior. Therefore, the SIBs still have a great distance away from practical applications. In the next decade, the success of SIBs will be strongly dependent on the development of efficient and safe anode materials.

3. Potassium ion batteries

Potassium salts are widely available in large quantities and at low cost. Potassium as anode material has a negative reductive potential of -2.93 V *vs.* SHE and a theoretical specific capacity of 591 mA h g^{-1} (Table 1). As the potential of potassium is similar to lithium, Potassium ion batteries (PIBs) are attracting increasing interest for energy storage. Some of the recently-reported electrode materials for PIBs are given in Table 4. To date, both aqueous and non-aqueous PIBs have been assembled, but most of reported PIBs show relatively low capacity and potential, this is why the research interests in PIBs is relative low [19,136]. Eftekhari has reported Prussian blue as a good material for K^+ storage [136]. The PIBs designed with potassium as anode and Prussian blue as cathode has a high cyclability for over 500 cycles. Furthermore, the chemical diffusion coefficient of K^+ in PIBs is higher than that of Li^+ in LIBs [137].

In 2011, Cui et al. synthesized nickel hexacyanoferrate (one of PBAs) in bulk quantity using spontaneous precipitation method under moderate temperatures [19]. They firstly described a rechargeable nickel hexacyanoferrate electrode on large size scale (~10 mg cm^{-2}) for PIBs and it showed little capacity loss after 5000 deep cycles at high current densities. In addition, they also prepared highly crystalline nanoparticles of copper hexacyanoferrate, another compound of PBAs, which showed high cycling life, rate capability, and round-trip energy efficiency as an electrode in PIBs with aqueous 1.0 M KNO_3 electrolyte [138].

Recently, Solanki et al. studied the size influence of Prussian blue and Prussian green particles on gravimetric capacity of PIBs [139]. They adjusted the size of Prussian blue particles (2–10 μm) and Prussian green particles (50–75 nm) by choosing different precursors. A reversible capacity of 30.27 mA h g^{-1} (44.7% of initial discharge capacity) was retained during galvanostatic cycling of the Prussian green at 500 mA g^{-1} for 1100 cycles. For the Prussian blue electrodes, 22.8% of initial discharge capacity of 49.16 mA h g^{-1} was retained. The Coulombic efficiency of Prussian blue and Prussian green electrodes was almost 100%.

Hu et al. reported that K^+ can electrochemically intercalate into graphitic materials, such as graphite and reduced graphene oxide at ambient temperature and pressure [140]. The electrochemical intercalation process clearly displays the formation of different stages in K-Graphite intercalation compounds. Graphite and reduced graphene oxide deliver a reversible capacity of 208 mA h g^{-1} and 222 mA h g^{-1} in nonaqueous electrolyte at 5 mA g^{-1}, respectively.

4. Magnesium ion batteries

Magnesium ion batteries (MIBs) are very attractive because magnesium has a low reduction potential of −2.37 V *vs.* SHE, a volumetric capacity (3832 mA h mL^{-1}) nearly twice than that of lithium (2026 mA h mL^{-1}) derived from the divalent nature, and relatively low cost originated from the high environmental abundance of magnesium resources (Table 1). More importantly, Mg does not form dendrites during reversible electrochemical plating/stripping, which dispels crucial safety concerns when used as an anode material [141]. Since the pioneering work of Aurbach and co-authors [142], MIBs have attracted increasing attention. Despite the promising features, the two biggest obstacles encountered by MIBs are the lack of suitable cathode materials in which Mg^{2+} can diffuse with fast kinetics and the lack of electrolytes compatible with electrodes. Herein, we provide a review section about the representative research of cathode and anode materials for MIBs.

4.1. Cathode materials

The development of cathode materials with high reversible capacity and adequate operating voltage under appropriate rate conditions is crucial for MIBs [143]. It is known that the kinetics of solid state diffusion through inorganic cathode materials is slow due to the high polarizing ability of the divalent Mg^{2+} cations, resulting in low reversible capacity and reduced power output. Up to now, there have been efforts to address these issues [144–146]. The typical cathode materials for MIBs are summarized in Table 5.

4.1.1. Chevrel phase Mo_6X_8 (X=S or Se)

In recent years, Chevrel phase compounds have been of particular interest as a possible cathode material for rechargeable MIBs, owing to its high tolerance for reversible Mg^{2+} insertion/extraction, high ionic conductivity and high density [147]. As shown in Fig. 14, six molybdenum atoms form an octahedron inside a cube of eight sulfur atoms [142]. A large number of short channels exist between multiple Mo_6S_8 clusters, which can easily compensate for the charge imbalance introduced by divalent ions. Mg^{2+} can possibly occupy two different sites between the lattices of Mo_6S_8,

Table 4
Electrochemical properties of typical electrode materials for PIBs reported in the literature.

Electrode materials	Ref.	Reversible capacity (mA h g^{-1})	Current density (mA g^{-1} or C)	Capacity retention
1. Cathode materials				
Prussian blue	[136]	87.36	0.1 C	88% after 500 cycles at 0.1 C
Nickel hexacyanoferrate	[19]	59	0.83 C	91.25% after 5000 cycles at 8.3 C
Copper hexacyanoferrate	[138]	60	0.83 C	83% after 40000 cycles at 17 C
Prussian green	[139]	123.1	111	44.7% and 22.8% after 1100 cycles at 500 mA g^{-1}, respectively
Prussian blue		53.8	111	
2. Anode material				
Graphite	[140]	208	5	–
Reduced graphene oxide		222	5	–

Table 5
Electrochemical properties of typical cathode materials for MIBs reported in the literature.

Electrode materials	Ref.	Reversible capacity (mA h g^{-1})	Current density (mA g^{-1} or C)	Capacity retention
$Mg_xMo_6S_{8-y}Se_y$ (y=0, 1, 2)	[148]	~110	C/8	–
$Cu_{0.1}$-doped VO_x-NTs	[155]	120.2	10	–
C-V_2O_5	[157]	600 mA h (g-V_2O_5)$^{-1}$	1 A (g-V_2O_5)$^{-1}$	–
α-MnO_2	[163]	280	36 μA cm^{-2}	–
λ-MnO_2	[164]	545.6	13.6	54% after 300 cycles at 136 mA g^{-1}
MoS_2	[169]	170	20	95% after 50 cycles at 20 mA g^{-1}
WSe_2	[173]	203	50	>90% after 160 cycles at 50 mA g^{-1}
TiS_2	[174]	236	10	78 after 80 cycles at 10 mA g^{-1}

as shown in the upper insert of Fig. 14. At the initial stage of Mg^{2+} insertion, the ions occupy the inner region (Site A) following the Reaction (4), and then the outer sites (Site B) accommodate further Mg^{2+} insertion following the Reaction (5):

$$Mo_6S_8 + Mg^{2+} + 2e^- \rightleftharpoons MgMo_6S_8 \quad (4)$$

$$MgMo_6S_8 + Mg^{2+} + 2e^- \rightleftharpoons Mg_2Mo_6S_8 \quad (5)$$

Although the Chevrel phase Mo_6S_8 exhibited excellent cycling performance (over 2000 cycles without significant loss) [142], some issues such as initial capacity loss (~15%) need to be resolved. One potential approach is to introduce Se (or Te) atoms into the compound; another possible way is to reduce the particle size of the sample. Recently, Levi et al. reported $Mo_6S_ySe_{8-y}$ cathode materials exhibiting higher mobility and faster reversibility [148]. They found that the reversible capacity was improved by the substitution of Se atoms (Fig. 15a and b) and no obvious capacity loss was shown during the cycling process. On the other hand, the electrochemical activity was effectively enhanced when the particle size of $Mo_6S_ySe_{8-y}$ was reduced (Fig. 15c and d).

4.1.2. Transition metal oxides

Another type of cathode materials for rechargeable MIBs is transition metal oxides. Compared with the Chevrel phase compounds, multiple transition metal oxides exhibit higher capacity and higher voltage (Fig. 16) [10].

V_2O_5 is a layered compound (Fig. 17a) which can provide pathways for Li^+ or Mg^{2+} insertion/extraction [149]. According to the reported literature [150,151], the diffusion of Mg^{2+} into the bulk V_2O_5 is slow, possibly due to the chemical modification of V_2O_5 crystal surface and its low electric conductivity. Great effort has been made to optimize the electrochemical performance of V_2O_5, including the control of crystallite size [152–155] and the use of conductive additives [156,157]. Reducing the particle size can decrease the diffusion pathway within the sample and improve the cycling performance. The addition of conductive materials, such as carbon materials, also can improve Mg^{2+} diffusion and increase reversible capacity [156,157]. It should be noted that the diffusion of Mg^{2+} can be facilitated by water molecules, because water can solvate Mg^{2+} and promote the insertion/extraction process [158]. However, water in the electrolyte also accelerates the formation of passivation film on the surface of Mg anode, thus unfavorable to the electrochemical performance.

MnO_2 with multiple polymorphs including tunneled MnO_2 (hollandite and todorokite), layered MnO_2 and spinel MnO_2 (Fig. 17b–e), is another promising cathode for MIBs due to its low cost and environment friendliness [159,160,162]. The severe problem of tunneled MnO_2 is the significant capacity loss caused by structural collapse of MnO_2 [163]. Layered MnO_2 can provide a two dimensional pathway for ions to intercalate and deintercalate. Although layered MnO_2 (birnessite phase) had a lower discharge capacity than tunneled MnO_2, it was able to retain more capacity after long cycles [159]. Recently, the electrochemical intercalation of Mg^{2+} into spinel MnO_2/graphite anode in the aqueous electrolytes of various magnesium compounds ($MgSO_4$, $Mg(NO_3)_2$ or $MgCl_2$) has been studied [164]. When the charge–discharge process was carried out in 1.0 M $MgCl_2$ electrolyte, an initial discharge capacity of 545.6 mA h g^{-1} was delivered and a capacity of 155.6 mA h g^{-1} was maintained after 300 cycles at the current density of 136 mA g^{-1}.

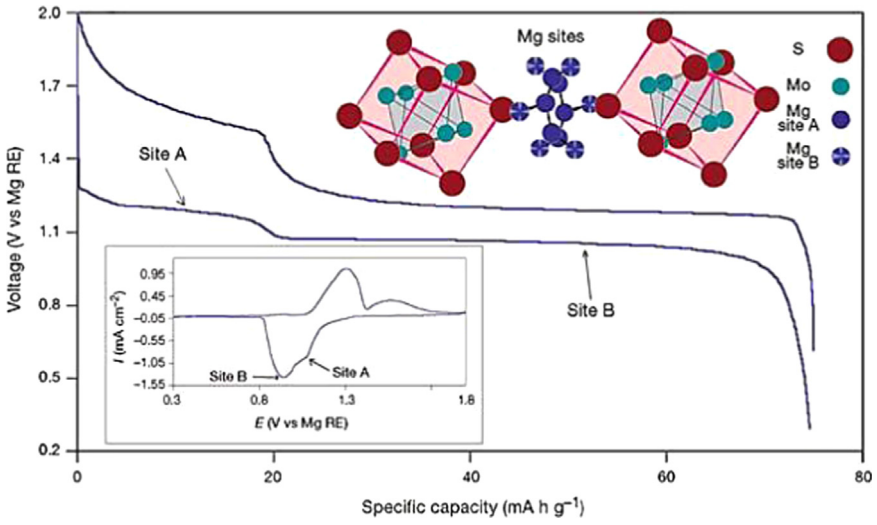

Fig. 14. Galvanostatic charge–discharge profiles of the Chevrel phase Mo_6S_8 cathode [142]. The insets show the crystal structure and cycle voltammogram of Chevrel phase Mo_6S_8.

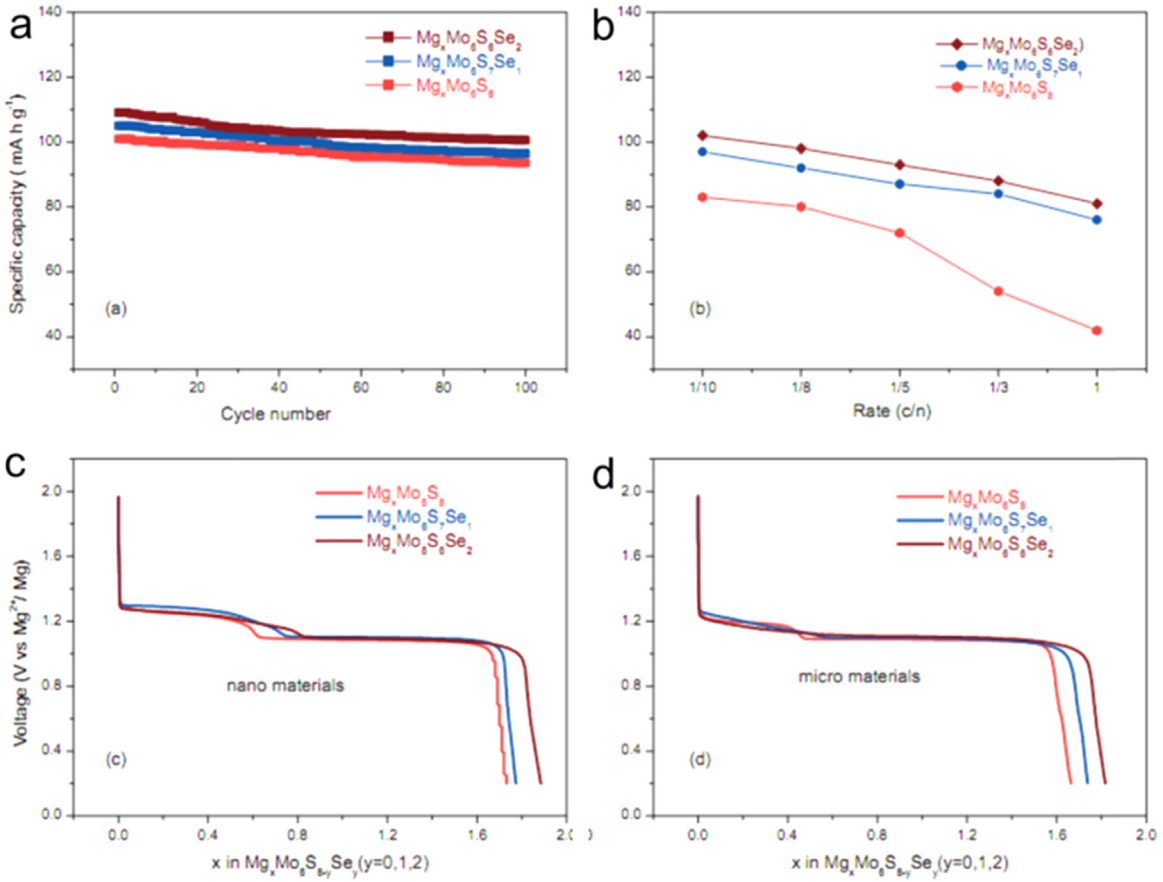

Fig. 15. (a) Cycling life and (b) Rate performance of $Mg_xMo_6S_ySe_{8-y}$ ($y=0$, 1, and 2) cathodes. Galvanostatic discharge profiles of (c) nano-sized and (d) micro-sized $Mg_xMo_6S_ySe_{8-y}$ (y=0, 1, and 2) cathode materials [148].

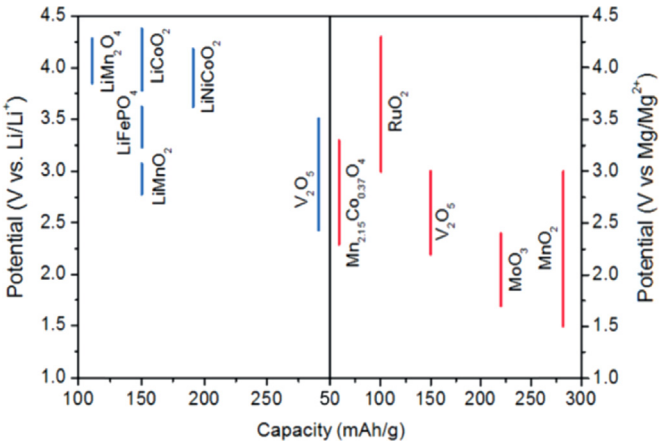

Fig. 16. The reaction potential of different transition-metal oxide cathodes for Li^+ or Mg^{2+} insertion/extraction [10].

4.1.3. MX_2 (M=metal; X=S or Se) type intercalation compounds

In recent years, layered MX_2 (M=Ti, Nb, Mo, W or V; X=S or Se) compounds have attracted more attention as cathode materials for MIBs. MoS_2 has long been recognized as a versatile electrode material [165,166] due to the weak van der Waals interaction between layers and the large interlayer distance, as shown in Fig. 18a [167]. MoS_2 with fullerene-like hollow-cage, fibrous floccus, and spherical nano-vesicle structures were employed as cathode material [168]. However, the cells usually exhibit low capacity, Coulombic efficiency and discharge voltage. The cathode reaction for MoS_2-based MIBs is as following:

$$6MoS_2 + 4Mg^{2+} + 8e^- \rightleftharpoons Mg_4Mo_6S_{12} \quad (6)$$

The Mg^{2+} hosting capability of MoS_2 has been investigated to refine new cathode material. Chen et al. reported a combination of highly-exfoliated graphene-like MoS_2 cathode and Mg nanoparticle anode [169], which exhibited an operating voltage of 1.8 V and a reversible discharge capacity of ~170 mA h g^{-1} after 50 cycles (Fig. 18b). The lattice fringe spacings of single- or few-layered MoS_2 were measured to be 0.65–0.70 nm, which are larger than those of bulk MoS_2 (0.63 nm). This work indicates the importance of rational morphology control of electrode materials.

So far, only a few Mg^{2+} insertion cathodes can present acceptable reversible capacity in MIBs. As a layer-structured metal chalcogenide, WSe_2 has some special characteristics, including ultralow thermal conductivity, highly-hydrophobic surface, and p-type field-effect properties [170–172]. For example, the preparation of WSe_2 nanowire-assembled film as a potential cathode for MIBs was reported [173]. The typical WSe_2 nanowires have an average diameter of ~100 nm, and the lattice spacings of (002) planes are ~0.65 nm. The WSe_2 electrode exhibited a specific capacity of ~200 mA h g^{-1} with Coulombic efficiency of ~98.5% over 160 cycles at 50 mA g^{-1} (Fig. 19a), and also good cycling stability at high current density of 1500 mA g^{-1} and 3000 mA g^{-1} (Fig. 19b).

TiS_2 is another possible candidate for the cathode of MIBs. Chen et al. have reported the TiS_2 nanotubes obtained by a low-temperature gas reaction method can reversibly intercalate and deintercalate Mg^{2+} in the channels derived from van der Waals interaction [174]. The TiS_2 nanotubes exhibited a discharge capacity of 236 mA h g^{-1} at 10 mA g^{-1} in the range of 2.0–0.5 V with a capacity retention of 78% over 80 cycles at 10 mA g^{-1}.

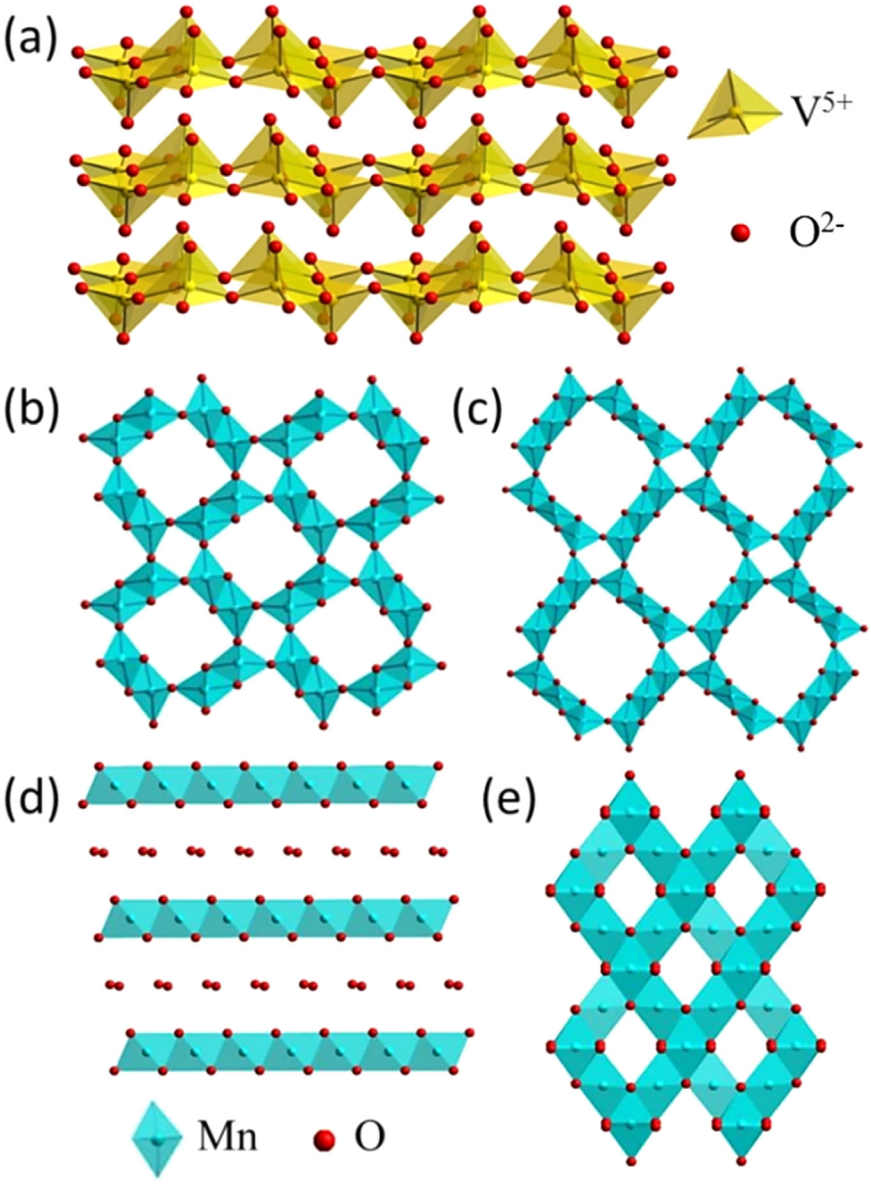

Fig. 17. Crystallographic structure of (a) crystalline V_2O_5 [149], (b) tunneled hollandite MnO_2 (2×2 tunnel) [159], (c) tunneled todorokite MnO_2 (3×3 tunnel) [160], (d) layered birnessite MnO_2 [161] and (e) spinel MnO_2 [162].

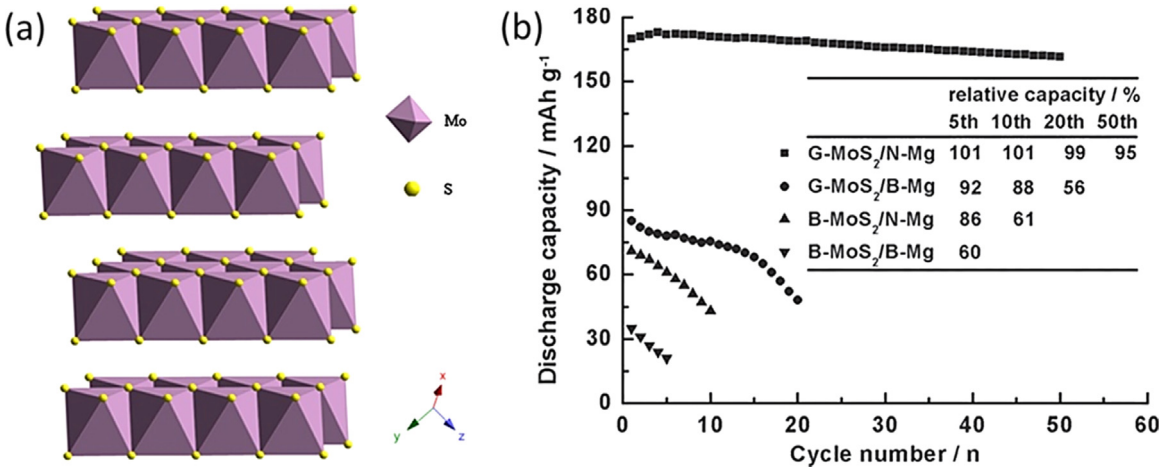

Fig. 18. (a) Crystalline structure of MoS_2 [167]. (b) Cycling capacity of MIBs based on graphene-like MoS_2 cathode and Mg nanoparticle anode at 20 mA g^{-1} [169]. The insert is the ratio of discharge capacity at the corresponding cycle to the initial capacity at the first cycle.

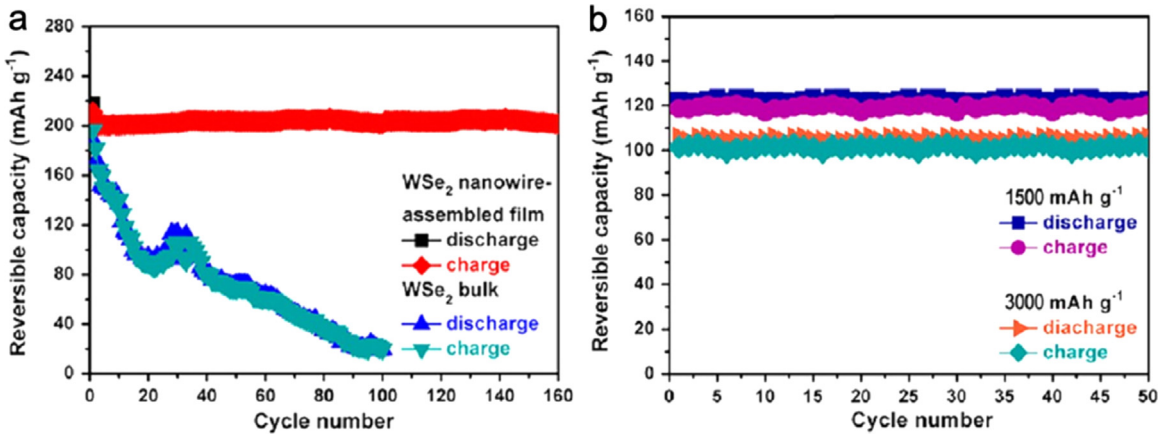

Fig. 19. (a) Cycling performance of the MIBs with WSe_2 nanowire-assembled film and WSe_2 bulk cathodes measured at 50 mA g^{-1} between 0.3 and 3.0 V. (b) Cycling performance of these electrodes at 1500 and 3000 mA g^{-1} [173].

Up to now, only a few cathode materials capable of reversible intercalation of Mg^{2+} have been developed, although their typical potential, rates, and specific capacities haven't reached the same levels of lithium ion cathodes. A main reason is the slow solid-state diffusion of Mg^{2+} which increases electrode polarization and results in possible ion trapping. Another reason is the possible co-intercalation of solvent molecules which may cause severe structural distortion and decompose within the cathode material. Due to the merits of MIBs mentioned above, the research for novel cathode materials with high capacity, potential and good rate performance has theoretical and practical significance.

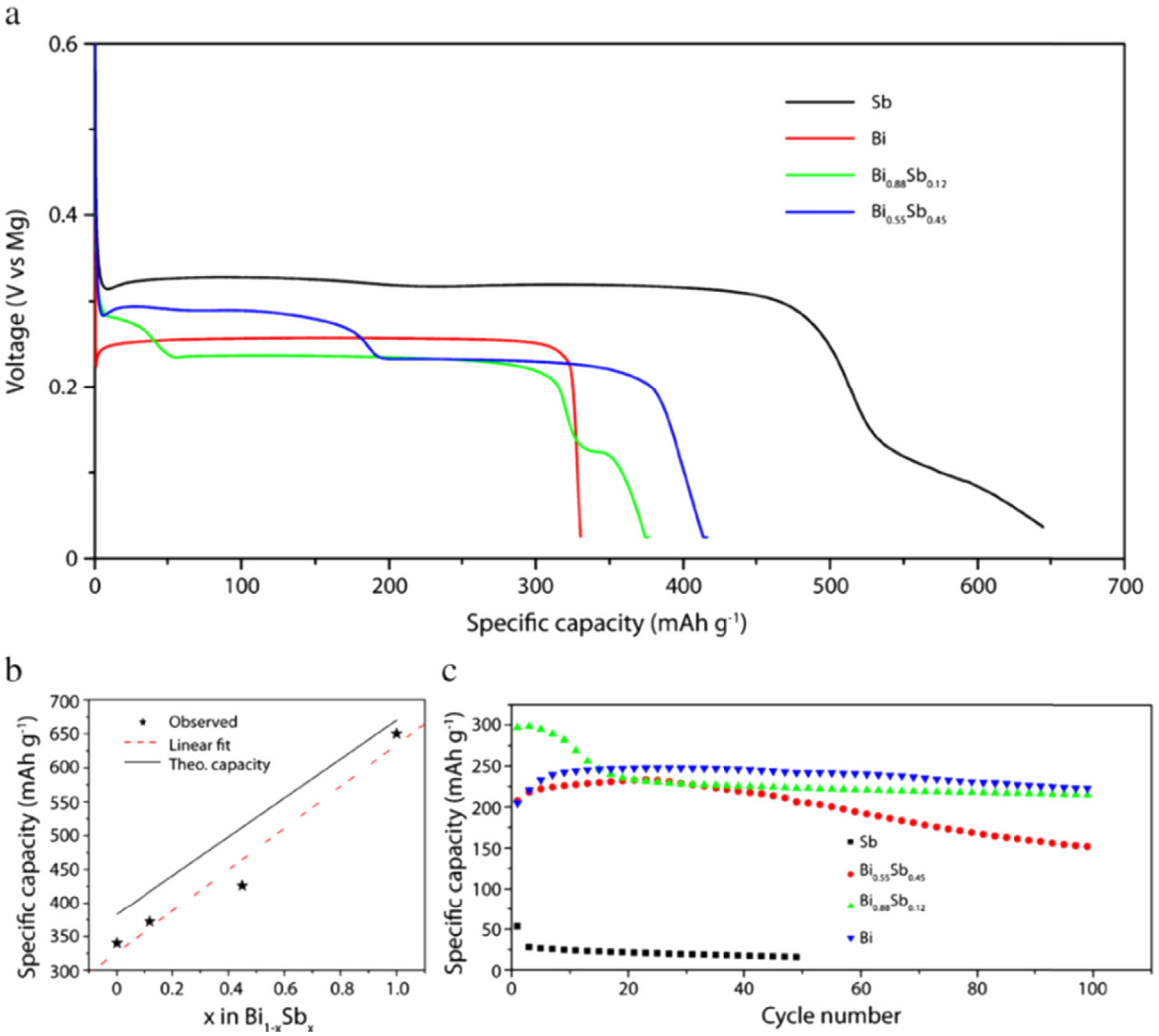

Fig. 20. (a) Discharge of Bi, Sb, $Bi_{0.88}Sb_{0.12}$ and $Bi_{0.55}Sb_{0.45}$ anodes at 0.01 C. (b) Observed capacities of $Bi_{1-x}Sb_x$ alloy anodes with a linear fit (dashed line) compared with the theoretical capacity (solid line) at 0.01 C. (c) Cycling performance of the above anodes at a 1 C [179].

4.2. Anode materials

4.2.1. Metal alloys

Clearly, Mg metal and alloys is one of the most suitable anodes for MIBs with high theoretical specific capacity (2205 mA h g^{-1}) and high electronegativity (−2.37 V *vs.* SHE) [142]. According to the literature [175,176], upon the decrease of Mg particle size, the capacity of both Mg/MnO_2 and Mg/Air batteries increased remarkably owing to the enhanced kinetics. Chen et al. reported the synthesis of ultrasmall Mg nanoparticles by ionic liquid-assisted chemical reduction method [169]. The electrochemical test in $Mg(AlCl_3Bu)_2$/tetrahydrofuran electrolyte indicated that Mg nanoparticles exhibited better performance than bulk Mg.

To date, the use of Mg metal as anode is still limited by the choice of electrolytes and the poor control of electrochemical reactions at metal–electrolyte interfaces [177,178]. In the case of LIBs, a series of new materials (such as Sn, Sn/C, Si and Si/C) have attracted considerable attention as high capacity anodes to replace graphite. Recently, similar researches about metals, alloys and intermetallic anodes for MIBs have also been reported. Matsui et al. reported Bi metal, Sb metal and $Bi_{1-x}Sb_x$ alloys as anodes for MIBs [179]. The authors proposed to improve the energy density by coupling the low reduction/oxidation potential of Bi with the high theoretical capacity of Sb. Both Bi and Sb films have grain sizes larger than 500 nm. $Bi_{0.88}Sb_{0.12}$ and $Bi_{0.55}Sb_{0.45}$ are comprised of 50–100 nm interconnected particles, while Sb films composed of 10–20 nm particles have a cauliflower-like morphology. Fig. 20a shows the discharge curves of $Bi_{1-x}Sb_x$ materials at 0.01 C rate. It also can be seen from Fig. 20b that the capacity of the anode at 0.01 C rate increases as x in $Bi_{1-x}Sb_x$ increases. At 1 C rate, $Bi_{0.88}Sb_{0.12}$ and Bi showed decent cycling capability over 100 cycles, while Sb failed to show appreciable capacity or cycle well at high rates regardless of the as-deposited morphology (Fig. 20c). These results indicate the bond strength of Mg–M (M=Bi or Sb) is very crucial to the electrochemical performance, which is consistent to a previous report that the ionicity of Mg_3Sb_2 is higher than Mg_3Bi_2, and the Mg–Sb bonding in Mg_3Sb_2 is stronger than the Mg–Bi bonding in Mg_3Bi_2 [180]. The proof-of-concept insertion/extraction of Mg^{2+} in Bi using a conventional electrolyte is an initial step towards extending the voltage window for MIBs.

It is well-known that nanostructured materials can improve the ion diffusion and structural stability of electrodes in LIBs [181,182], and similar situation can also be applied to MIBs. Bulky bismuth offers specific capacity of 385 mA h g^{-1} but undergoes ~100% volume expansion during the formation of Mg_3Bi_2. Recently, Liu et al. showed that Bi nanotubes can be used as anode material to

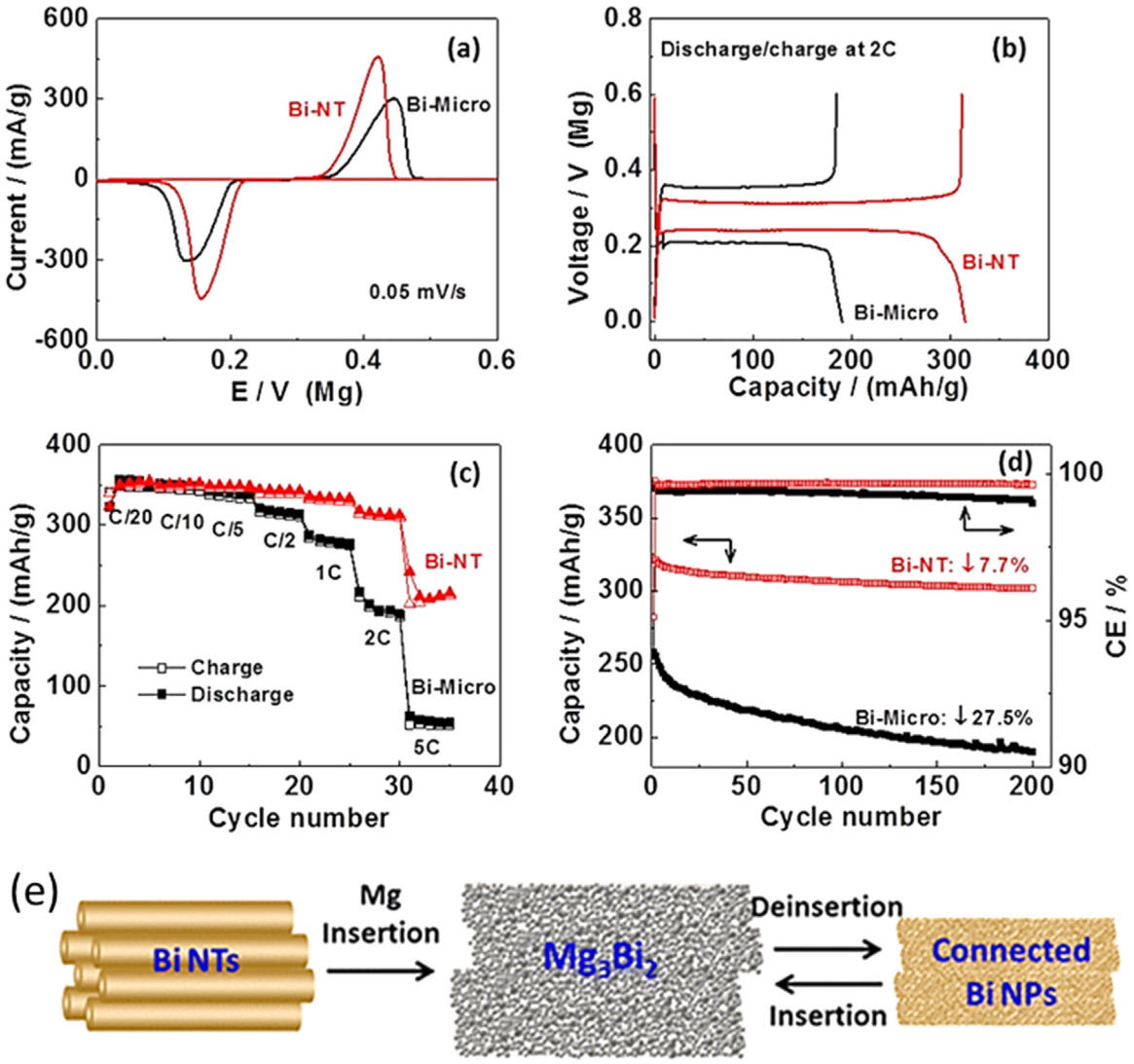

Fig. 21. (a) Cyclic voltammogram of Mg insertion/deinsertion in bismuth. (b) discharge–charge profile of an Mg–Bi cell. (c) rate performance of an Mg–Bi cell. (d) cycling stability and Coulombic efficiency (CE) of Mg^{2+} insertion/extraction. (e) Structural transformation of Bi nanotubes during the charge–discharge process [183].

buffer the volume expansion [183]. The following is the Bi–Mg alloying reaction:

$$2Bi + 3Mg^{2+} + 6e^{-} \rightleftharpoons Mg_3Bi_2 \quad (7)$$

In this work, Bi nanotubes and Bi microparticles (~100 μm) were respectively used as anodes for MIBs. The cycle voltammogram of Bi nanotubes (Fig. 21a) exhibits highly symmetric cathodic/anodic peaks and narrower peak separation than that of Bi microparticles (0.264 V *vs.* 0.313 V), indicating highly reversible and fast insertion/extraction of Mg^{2+} in Bi nanotubes. The performances of Bi nanotubes are much better than Bi microparticles (Fig. 21b–d). The authors suggested that the hollow space in Bi nanotubes accommodated volume change and prevented structural collapse of the electrode. Moreover, the highly interconnected Bi nanoparticles formed along the Bi nanotubes provided good electric contact (Fig. 21e).

To possess a large capacity and low intercalation voltage is very important for anode materials. Recently, Sn powder film electrodes were compared with Bi as anodes for MIBs [184]. The results have shown that Sn has lower Mg^{2+} insertion/extraction voltage (~0.15/0.20 V) and larger initial discharge capacity (close to the theoretical capacity of 903 mA h g^{-1} at 0.002 C). However, the specific capacity in the initial opposite scan process was only about 350 mA h g^{-1}. The poor Coulombic efficiency was attributed to the severe volume expansion during the transformation from Sn to Mg_2Sn phase. The diffusion of Mg atom in α-Sn and β-Sn was investigated using density functional theory [185]. The first-principles calculation showed that the energy barriers for Mg atom in the α-Sn and β-Sn were 0.395 and 0.435 eV, respectively (Fig. 22). Furthermore, the addition of a second Mg atom (enclosed by a red cycle shown in Fig. 22b) decreased the diffusion barrier in α-Sn while increased the diffusion barrier in β-Sn, indicating α-Sn is a better candidate than β-Sn as anode material for MIBs.

4.2.2. *Low-strain metal oxides*

Recently, spinel $Li_4Ti_5O_{12}$ with low-strain characteristic was demonstrated as promising Mg^{2+}-insertion anode [186]. The *in-situ* synchrotron XRD (Fig. 23) shows that the peak intensities of cycled electrode increased slightly, but no obvious peak shifts or new Bragg reflections were observed, indicating small volume changes during the charging/discharging process. The result might be attributed to the comparable effective ionic radii of Mg^{2+} (0.72 Å) and Li^{+} (0.76 Å). The reversible capacity of $Li_4Ti_5O_{12}$ gradually increases during the initial cycles and reaches a maximum value of 175 mA h g^{-1} in the 15th cycle (Fig. 24a). After 15 cycles, the shape of charge–discharge curve changed from a plateau to a sloped line (Fig. 24b). The reversible capacity becomes lower at high rates (Fig. 24c), implying the kinetics of Mg^{2+} diffusion is relatively sluggish because of the high polarizing power [144,157,174,187]. $Li_4Ti_5O_{12}$ nanoparticles exhibit good cycling stability and Coulombic efficiency at the current density of 300 mA g^{-1} for 500 cycles (Fig. 24d), which was attributed to the zero-strain characteristic of $Li_4Ti_5O_{12}$.

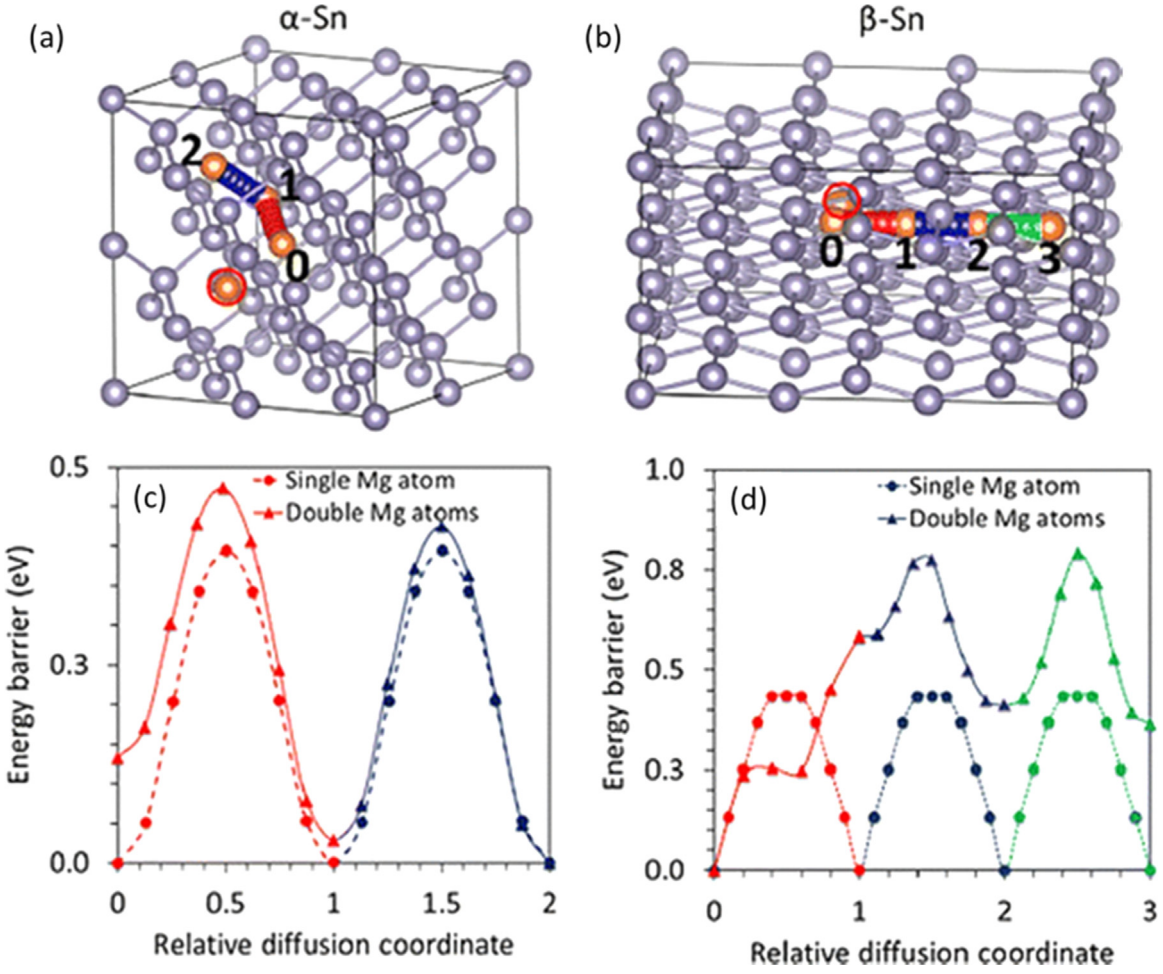

Fig. 22. The diffusion paths and energy curves for Mg diffusion between the adjacent stable sites in (a, c) α-Sn and (b, d) β-Sn, respectively. The dashed line shows a single Mg diffusion, and the solid line shows the diffusion of two Mg atoms [185]. (For interpretation of the references to color in this figure, the reader is referred to the web version of this article.)

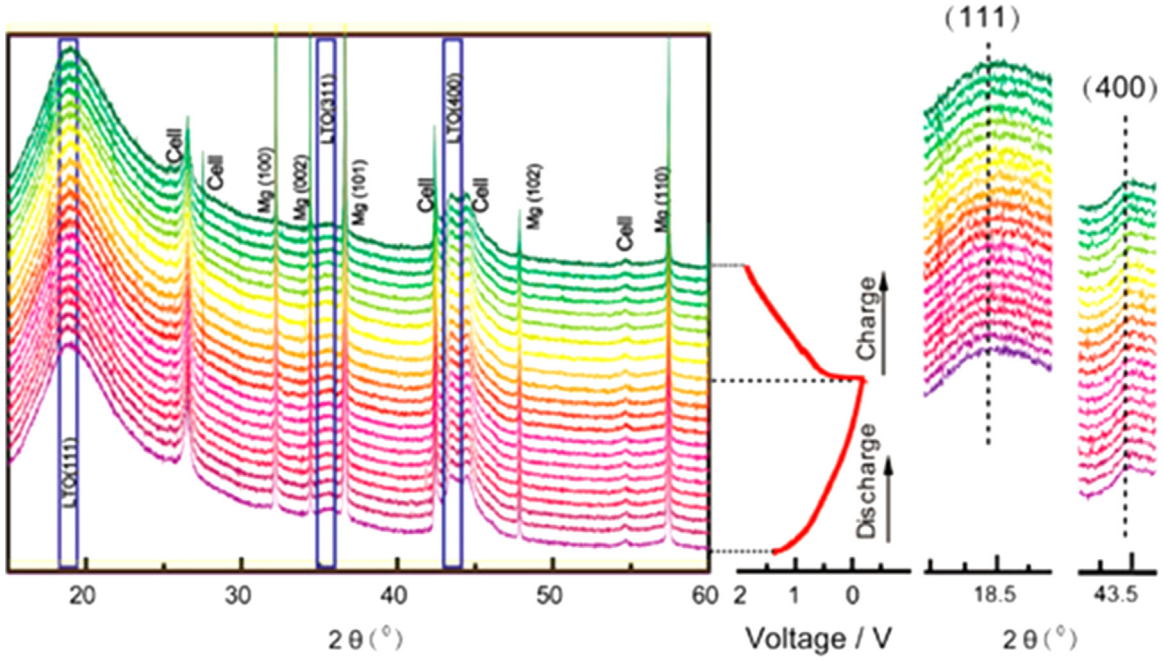

Fig. 23. *In-situ* XRD patterns collected during the first discharge–charge cycle of the $Li_4Ti_5O_{12}$/Mg cell under a current rate of 0.1 C between 0–1.85 V [186].

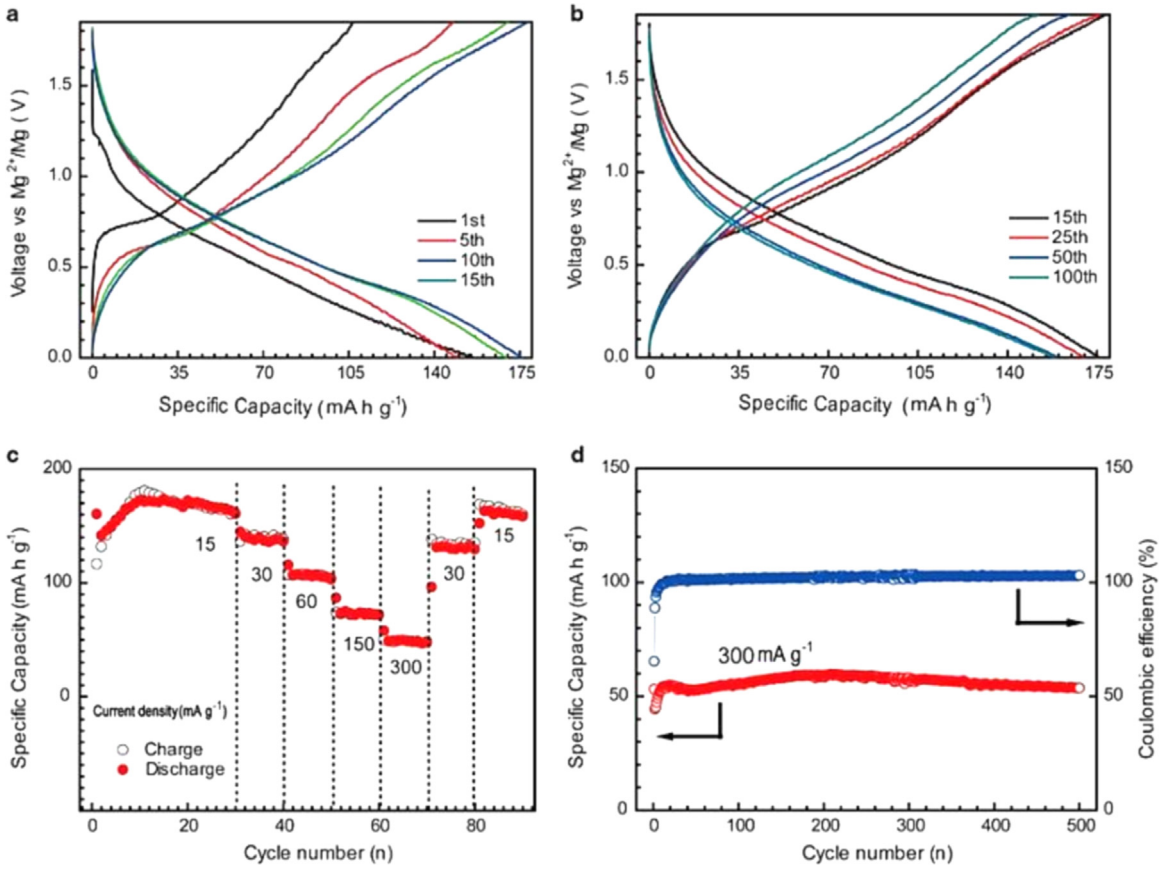

Fig. 24. Charge–discharge profiles of $Li_4Ti_5O_{12}$ electrodes in MIBs (a) before and (b) after 15 cycles at 15 mA g^{-1}. (c) Rate capabilities at different current densities. (d) Cycling performance at 300 mA g^{-1} [186].

Overall, the anode materials for MIBs have been investigated to a limited extent, as summarized in Table 6. Mg metal itself can serve as anode, but in this case the possible electrolytes will be mostly narrowed to Grignard reagents and ethereal solvents. If the electrolyte is inappropriate, a passivating layer insulating the Mg^{2+} trends to form at the surface of highly-reactive Mg metal owing to the side reactions. Therefore, it is necessary to develop novel anode materials. The recent development of Mg alloy and low-strain compound anodes provides opportunities for the use of more conventional electrolytes, although there are still many challenges yet to overcome.

Table 6
Electrochemical properties of typical anode materials for MIBs reported in the literature.

Electrode material	Ref.	Reversible capacity (mA h g^{-1})	Current density (mA g^{-1} or C)	Capacity retention
$Bi_{0.88}Sb_{0.12}$	[179]	298	1 C	72% after 100 cycles at 1 C
Bi	[183]	350	0.05 C	92.3% after 200cycles at 0.05 C
Sn	[184]	903	0.002 C	–
$Li_4Ti_5O_{12}$	[186]	175	15	95% after 500 cycles at 300 mA g^{-1}

5. Calcium ion batteries

Calcium-ion batteries (CIBs) have received increasing attention because Ca element is the fifth most abundant element in the Earth's crust and has a high volumetric capacity of 2073 mA h mL^{-1} (Table 1). Ca^{2+} has an ionic radius larger than Li^+ and lower reduction potential of −2.87 V *vs.* SHE (~0.17 V more positive than Li^+) [21]. Besides, calcium metal is less malleable than lithium, which affords the possibility for uniform deposition and avoids the growth of dendrite during charges/discharge cycles. Nevertheless, CIBs still face some serious problems. While the development of electrolytes for some other multivalent metals (such as Zn and Al) had a long history, the electrolytes for Ca^{2+} transport received far less attention. In 1991, Aurbach et al. investigated the behavior of calcium electrodes in electrolytes containing organic solvents and salts [188]. They have concluded that calcium deposition cannot occur in many electrolyte systems comprising of $Ca(ClO_4)_2$ and organic solvents. This is possibly due to the formation of a passive layer derived from the reduction of salt and/or solvent, which is apparently nonconductive for Ca^{2+} ions.

The lack of suitable calcium electrolytes hindered the investigation of electrode materials for CIBs. Table 7 lists several typical electrode materials for CIBs demonstrated in the literature. Jaworski et al. reported that crystalline vanadium oxides could host multivalent cations, such as Ca^{2+}, Mg^{2+}, and Y^{3+} [152]. Sakurai et al. also investigated the insertion/extraction behavior of Ca^{2+} in vanadium oxides by using $Ca(ClO_4)_2$/acetonitrile solution [189].

Recently, Solanki et al. reported potassium barium hexacyanoferrate ($K_2BaFe(CN)_6$, one of PBAs) as a cathode for Ca^{2+} intercalation (Fig. 25) [21]. By introducing a small proportion of deionized water into organic electrolyte, the intercalation/de-intercalation of Ca^{2+} was significantly enhanced, which implies that the resistance barrier for Ca^{2+} intercalation from electrolyte into $K_2BaFe(CN)_6$ was reduced, leading to an improved reversible capacity of 55.8 mA h g^{-1} with a Coulombic efficiency of ~93.8% at the 30th cycles.

Table 7
Electrochemical properties of typical electrode materials for CIBs reported in the literature.

Electrode material	Ref.	Reversible capacity (mA h g^{-1})	Current density (mA g^{-1})	Capacity retention
1. Cathode materials				
$K_2BaFe(CN)_6$	[21]	55.8	12.5	–
V_2O_5	[152]	200	–	–
V_2O_5	[189]	>400	0.05 mA cm^{-2}	–
2. Anode materials				
Grapheme	[190]	2142 or 2900 for different defects (theoretical)	–	–
Ti_3C_2 MXene	[191]	319.8 (theoretical)	–	–

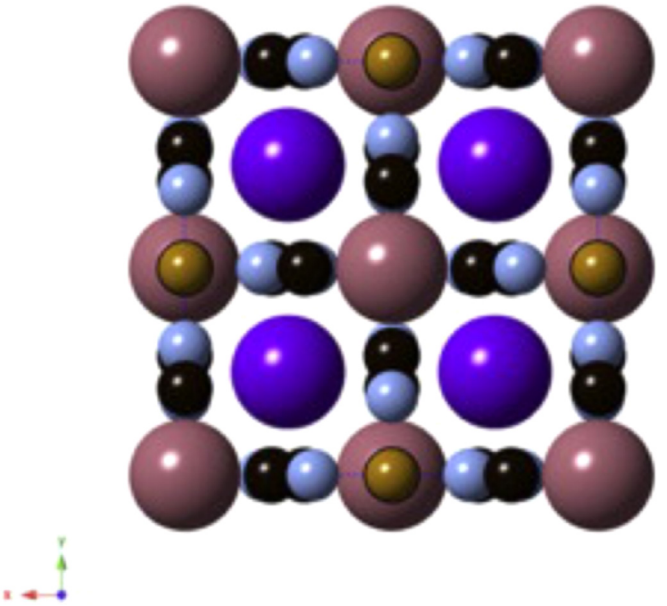

Fig. 25. Crystal structure of $K_2BaFe(CN)_6$ represented by spheres in purple (Ba^{2+}), brown (Fe^{2+}), light blue (CN^-), black (CN^-) and blue (K^+ in the interstitial sites) [21]. (For interpretation of the references to color in this figure legend, the reader is referred to the web version of this article.)

Shenoy and co-workers investigated the influence of the divacancy and Stone–Wales defects in graphene on the adsorption of Na and Ca by first-principles calculations based on density functional theory [190]. Enhanced adsorption can be seen on the defective graphene due to increased charge transfer between adatoms and defects. Their results provide a possible way to design of high-capacity anode materials for SIBs and CIBs. They also calculated the possibility of Ti_3C_2 MXene as an anode material for different metal (Li, Na, K, and Ca) ion batteries [191]. The calculated capacities for Li, Na, K, and Ca were respectively 447.8, 351.8, 191.8, and 319.8 mA h g^{-1}, showing MXenes could be promising for increasing the capacity of CIBs.

6. Zinc ion batteries

Zinc ion battery (ZIBs) is a new class of energy storage device with unique merits of fast charge–discharge capability, high power density and energy density, good safety and environmental benignity [192]. The reduction potential of Zn is -2.20 V *vs.* SHE (Table 1). Due to the rich natural abundance of Zn metal, ZIBs is attracting rising attention for potential applications. Metal Zn was usually used as the anode part of ZIBs. However, appropriate cathode materials allowing reversible insertion of divalent Zn^{2+} in aqueous electrolytes are very limited so far, which greatly hinders the development of aqueous ZIBs. Therefore, much effort has been devoted into the design of novel cathode materials [192]. The typical cathode materials for ZIBs reported in the literature are listed in Table 8.

Zn/MnO_2 battery is the most intensively investigated ZIB systems, which stores energy *via* conversion reactions attributed to the existence of a variety of oxidation states of MnO_2. In the 1860 s, a Zn/α-MnO_2 battery with alkaline KOH electrolyte was firstly fabricated, and it paves the road for secondary ZIBs [193]. In the subsequent years, several Zn/MnO_2 battery systems with different types of MnO_2 were prepared [23,192,194–196]. As shown in Fig. 26, the Zn/γ-MnO_2 battery delivers a high initial discharge

Table 8
Electrochemical properties of typical cathode materials for ZIBs reported in the literature.

Electrode material	Ref.	Reversible capacity (mA h g^{-1})	Current density (mA g^{-1} or C)	Capacity retention
α-MnO_2	[192]	210	0.5 C	~100% after 100 cycles at 6 C
γ-MnO_2	[23]	285	0.05 mA cm^{-2}	55% after 40 cycles at 0.05 mA cm^{-2}
Todorokite-type MnO_2	[194]	108	0.5 C	–
α-MnO_2	[195]	195	C/20	70% after 30 cycles at C/5
MnO_2	[196]	210	200	~100% after 50 cycles at 1 A g^{-1}
MnO_2/carbon nanotubes	[197]	1402	200	77% after 50 cycles at 200 mA g^{-1}
MnO_2/acid-treated carbon nanotubes	[199]	540	500	~100% after 500 cycles at 5 A g^{-1}
$Na_{0.95}MnO_2$	[200]	60	2 C	92% after 1000 cycles at 4 C
MnO_2/carbon fibers	[201]	158	70	–
copper hexacyanoferrate	[202]	56	20	77% after 20 cycles at 20 mA g^{-1}
NiOOH	[203]	20 mA h cm^{-2}	10 mA cm^{-2}	–
Ni foam-supported polyaniline	[207]	183.28	2.5 mA cm^{-2}	–

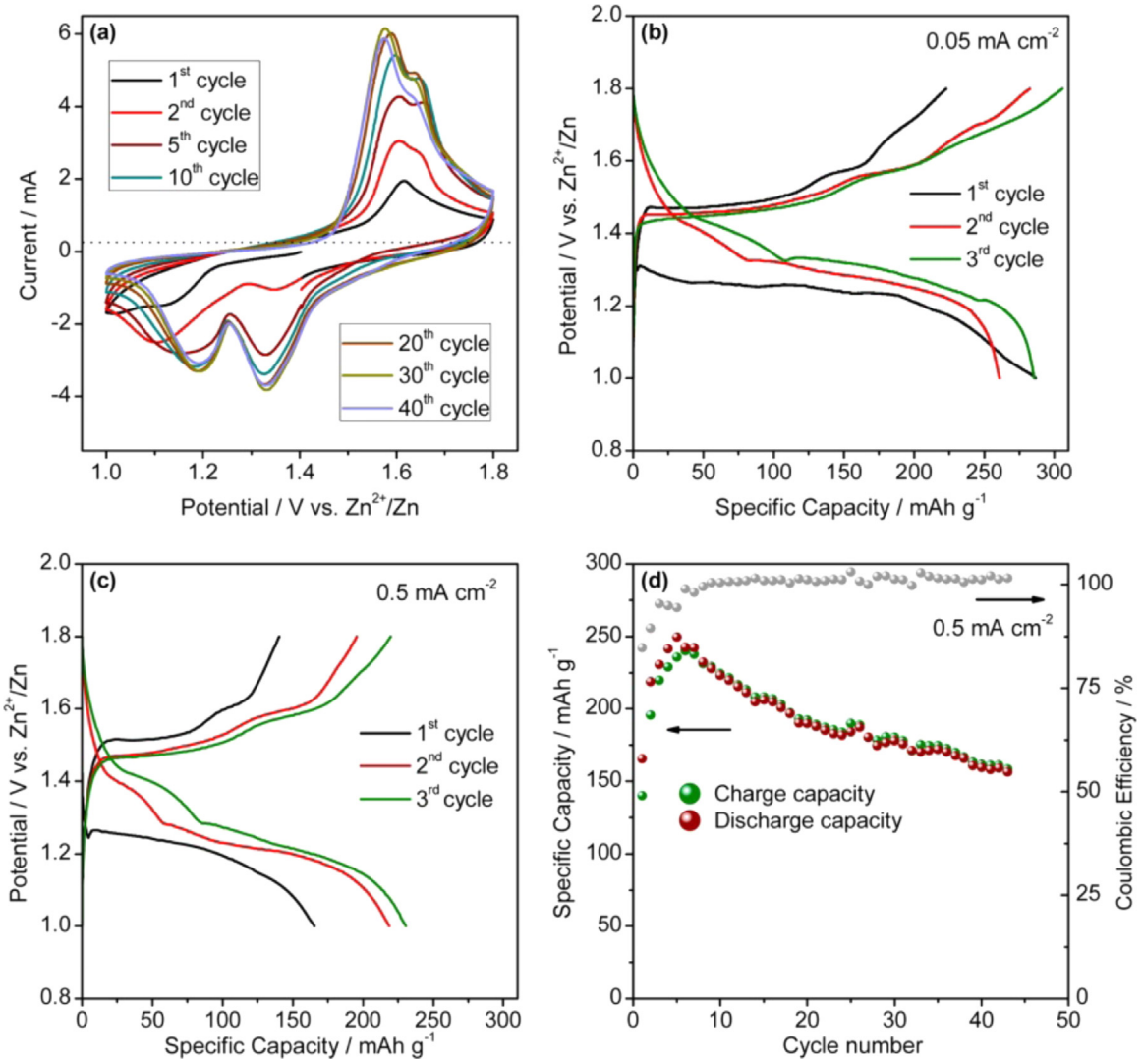

Fig. 26. (a) Cyclic voltammogram of Zn/γ-MnO_2 battery at different intervals until 40 cycles. The initial three voltage profiles were cycled at (b) 0.05 and (c) 0.5 mA cm^{-2} within 0.8–1.8 V. (d) The cycle performance of Zn/γ-MnO_2 battery within 0.8–1.8 V at 0.5 mA cm^{-2} [23].

capacity of 285 mA h g^{-1} at 0.05 mA cm^{-2} with a clear plateau at around 1.25 V *vs.* Zn/Zn^{2+} [23]. However, although the Zn/MnO_2 batteries have been widely employed in portable electronic devices, the fast capacity decay and low Coulombic efficiency originated from the poor electrical conductivity of MnO_2 seriously influence their performances. Carbon nanotubes are considered as an ideal additive to improve electrical conductivity of MnO_2 based electrodes [197,198]. For example, MnO_2 nanorods were *in-situ* deposited on the surface of acid-treated carbon nanotubes to form MnO_2/carbon nanotube composites for Zn^{2+} storage in a mild aqueous system [199]. The composites display both good energy capacity (~400 mA h g^{-1} at 1 A g^{-1}) and reversibility at various current densities (~100% Coulombic efficiency after 500 charge/discharge cycles). Other cathode materials based on MnO_2 was also prepared, such as $Na_{0.95}MnO_2$ [200] and MnO_2/carbon fiber composites [201].

Many novel cathode materials beyond MnO_2 were fabricated recently. For example, Jia et al. developed a copper hexacyanoferrate cathode material with well-defined open framework [202]. The results showed that Zn^{2+} can be reversibly inserted into/extracted from this cathode in aqueous solution due to its small radius. A Zn/NiOOH battery proposed by Cheng et al. showed that high efficiencies can be achieved with an average Coulombic efficiency of 96% and energy efficiency of 86% over 1000 cycles [203]. Some organic cathode materials, such as polyaniline and polyaniline/Ni foam, were also developed for ZIBs [204,205]. Compared with common inorganic cathode materials, the organic cathode materials exhibit some advantages, such as ecological acceptability, low cost and facile manufacture. Grgur et al. found polyaniline-based electrodes in chloride containing electrolytes with the addition of citrate anions showing better discharge performance with a maximum discharge capacity of 164 mA h g^{-1} [206]. Si and co-workers prepared a nickel foam supported polyaniline cathode with improved specific capacity (up to 183.28 mA h g^{-1} at the current density of 2.5 mA cm^{-2}) *via* the assistance of electrophoretic interlayer [207].

In short, rechargeable ZIBs are usually made up of environmentally friendly and safe materials and can be assembled by facile battery techniques. Therefore, ZIBs have been considered as one of the potential candidates for replacing LIBs. But there are several drawbacks need to be avoided, such as limited choices of appropriate cathode materials allowing reversible insertion of divalent Zn^{2+}, insufficient discharge capacity, and shot cycle life.

7. Aluminum ion batteries

Aluminum is the most abundant metal in the Earth's crust. Rechargeable aluminum ion batteries (AIBs) have the advantages of low cost and low flammability, together with three-electron-redox properties resulting in high capacity [208]. The multivalent nature of Al endows itself with a volumetric capacity of 8040 mA h L^{-1} (Table 1). However, aluminum has a high reduction potential of −1.67 V *vs.* SHE. Meanwhile, the specific capacity and cycle life are not as good as expected, which are mainly caused by aluminum corrosion and side reactions between the electrolyte and the cathode. Therefore, the design of compatible electrolytes and electrodes is of great importance for AIBs. In the previous reports, metal Al usually served as anode material for AIBs. The existing cathode materials developed for AIBs are summarized in Table 9.

Aqueous solutions can be used as electrolytes in AIBs. Gao et al. demonstrated that Al^{3+} can be reversibly inserted into/extracted from anatase TiO_2 nanotube arrays in aqueous $AlCl_3$ solution due to the small radius of Al^{3+} [209]. Liu et al. claimed that Cl^- could play a key role during charge/discharge cycles and the insertion of Al^{3+} into TiO_2 nanotube arrays was helpful for the reduction of Ti^{4+} to Ti^{3+} [210]. Similarly, Tong et al. used mesoporous black anatase TiO_2 nanoleaves as cathode and $Al(NO_3)_3$ solution as electrolyte to assembly AIBs, which showed a capacity of 278.1 mA h g^{-1} at 0.05 A g^{-1} and exhibit a good rate capability [211]. Copper hexacyanoferrate was also investigated as cathode [212]. The Al^{3+} insertion was identified by XRD measurement and the framework of copper hexacyanoferrate was stable during the Al^{3+} insertion/extraction processes. Nevertheless, the reduction of Al^{3+} in aqueous solutions is problematic owing to some side effects such as hydrogen evolution reaction [209]. The available voltage window gets narrow, which may results in a lower specific capacity. Therefore, the development of novel non-aqueous electrolytes is of great importance for AIBs.

Ionic liquids, composed of ions entirely, are nonvolatile, nonflammable, heat-stable, conductive and miscible with many organic solvents. Due to their wide electrochemical window and high conductivity, they are widely used in electrolytes and environmental friendly solvents. Jiao et al. proposed a battery with Al foil anode, VO_2 cathode and ionic liquid based electrolyte (1:1 M ratio of $AlCl_3$ and 1-butyl-3-methylimidazolium chloride mixture with ~0.5 wt% benzyl sulfoxide as corrosion inhibitor) [213]. The battery in this work showed an initial discharge capacity of 165 mA h g^{-1} and 116 mA h g^{-1} after 100 cycles at the current density of 50 mA g^{-1}. Nevertheless, side reactions are still limiting the performance of AIBs, even if the ion liquid based electrolytes are used. Rechargeable AIBs were also fabricated by applying V_2O_5 nanowire cathode and $AlCl_3$/ion liquid electrolyte, presenting an initial discharge capacity of 305 mA h g^{-1} and 273 mA h g^{-1} after 20 cycles [208]. However, the voltage was much lower than expected, which could be caused by side effects. Menke et al. used V_2O_5 as cathode, stainless steel as current collector and 1-ethyl-3methylimidazolium chloride solution of $AlCl_3$ as electrolyte [214]. The authors found the V_2O_5 shows electrochemical inactivity between 5 mV and 1.5 V *vs.* Al/Al^{3+} and the battery performance is independent of V_2O_5 but entirely up to the stainless steel. However, Bai et al. delivered an opposite conclusion [215]. They directly deposited V_2O_5 on Ni foam current collector to form the cathode. The discharge capacity of this cell is much higher than that of using a cathode consisting of V_2O_5 nanowires and binder. They also found that if only using Ni foam as cathode, there is no electrochemical activity in the cell. Therefore, it is V_2O_5 participated in the redox reaction. Moreover, when using $AlCl_3$/1-butyl-3-methylimidazolium chloride solution as electrolyte, polyvinylidene fluoride is unsuitable for binder and polytetrafluoroethylene is better.

Several polymers capable of electrochemical oxidation/reduction in electrolyte solutions were used as electrode materials for AIBs [216]. Hudak demonstrated rechargeable AIBs with polypyrrole or polythiophene as conducting polymer cathodes, showing stable cycle performance and electrode capacities near theoretical levels [217]. However, the value of practical voltage was

Table 9
Electrochemical properties of typical cathode materials for AIBs reported in the literature.

Electrode material	Ref.	Reversible capacity (mA h g^{-1})	Current density (mA g^{-1})	Capacity retention
V_2O_5	[208]	305	125	90% after 20 cycles at 125 mA g^{-1}
Anatase TiO_2 nanotube arrays	[209]	75	4 mA cm^{-2}	–
TiO_2 nanotube arrays	[210]	74.8	4 mA cm^{-2}	–
TiO_2 nanoleaves	[211]	278.1	50	91.6% after 300 cycles at 50 mA g^{-1}
Copper hexacyanoferrate	[212]	62.9	50	54.9% after 1000 cycles at 400 mA g^{-1}
VO_2	[213]	165	50	70% after 100 cycles at 50 mA g^{-1}
Bind-free V_2O_5	[215]	239	44.2	–
Polypyrrole	[217]	~70	20	74% after 100 cycles at 20 mA g^{-1}
Polythiophene	[217]	85	16	87% after 100 cycles at 20 mA g^{-1}
Fluorinated natural graphite	[219]	225	60	–
3D graphitic-foam	[22]	65	66	~100% after 7500 cycles at 4 A g^{-1}

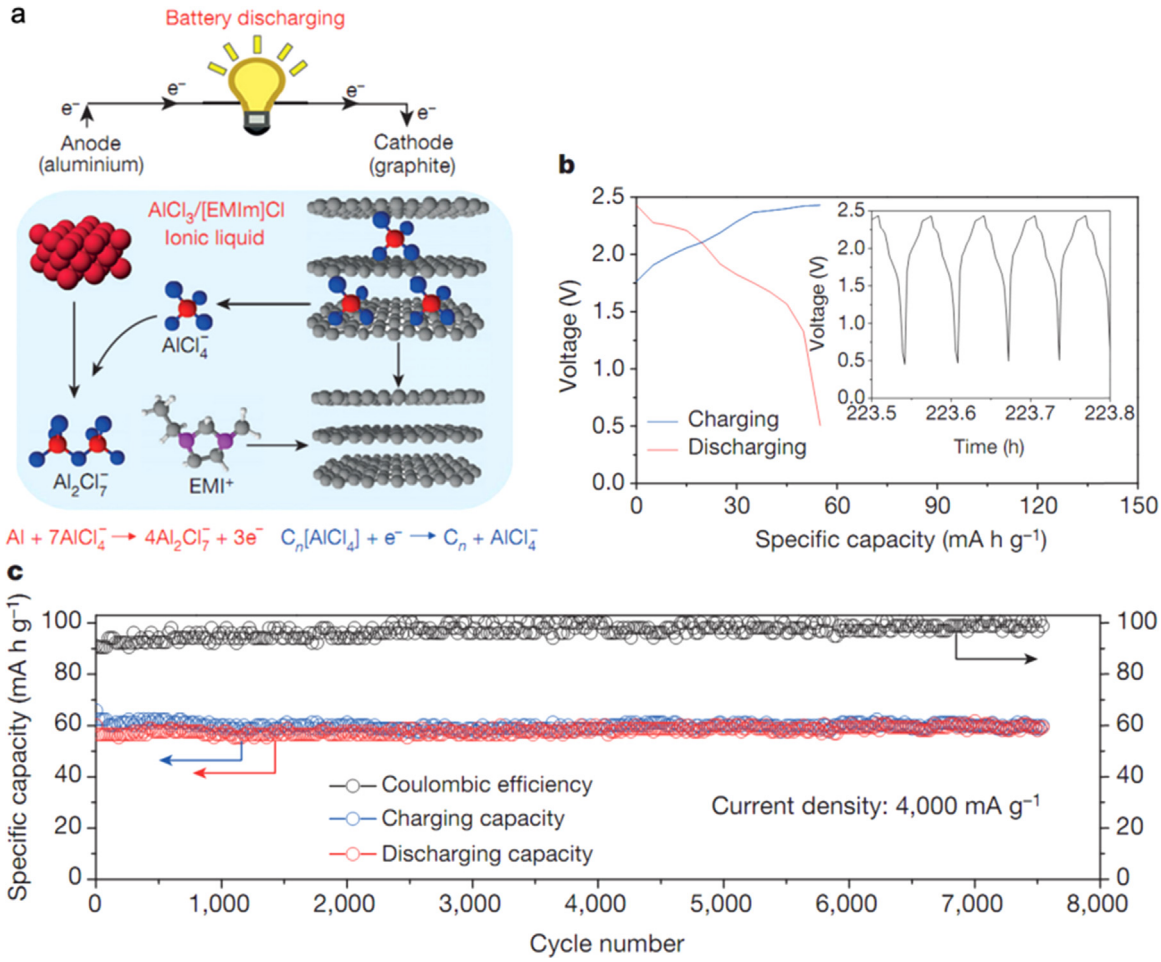

Fig. 27. (a) Scheme of the Al/graphite cell during discharge process. Al and $AlCl_4^-$ were converted to $Al_2Cl_7^-$ on the anode side and $AlCl_4^-$ was de-intercalated from graphitic interlayers on the cathode side. (b) Galvanostatic charge and discharge curves of an Al/graphitic-foam pouch cell at 4 A g^{-1}. (c) Stability test of an Al/graphitic-foam pouch cell at 4 A g^{-1} [22].

limited by the significantly sloping voltage profiles during charging/discharging. Furthermore, low Coulombic efficiency and irreversible reactions leading to capacity loss would occur at high voltages.

The compatibility between the electrolyte and cathode should be considered for the design of AIBs. Graphite fluoride material (C_x F, $2 < x < 5$) prepared in the presence of liquid hydrogen fluoride was reported to be an electrical conductor superior to graphite and also suitable for reversible fluorine intercalation [218]. Rani et al. demonstrated a rechargeable AIB with fluorinated natural graphite cathode, presenting a discharge capacity of 225 mA h g^{-1} and stable performance for 40 cycles [219].

Large complex ion radius and high multivalent ion charge concentration often lead to poor kinetics in multivalent-ion batteries, thus it is difficult to find proper host materials to serve as fast intercalation cathodes. Recently, Dai et al. demonstrated an ultrafast AIB system combining an Al foil anode, a porous graphitic-foam cathode and an $AlCl_3$/1-ethyl-3-methylimidazolium chloride electrolyte, as shown in Fig. 27a [22]. The redox reactions of the battery during charging and discharging can be written as:

$$4Al_2Cl_7^- + 3e^- \rightleftharpoons Al + 7AlCl_4^- \quad (8)$$

$$C_n + AlCl_4^- \rightleftharpoons C_n[AlCl_4] + e^- \quad (9)$$

The battery can be charged in ~1 min at the current density of ~4 A g^{-1} (Fig. 27b) and maintains a discharge capacity of 60 mA h g^{-1} for 7500 cycles with a Coulombic efficiency of 97 ± 2.3% (Fig. 27c). The graphitic-foam cathode was found to allow fast anion diffusion and intercalation. However, the specific capacity is still relatively low for practical use.

8. Conclusion and perspective

The urgent requirement to fabricate energy storage materials and devices with high energy density and rate capability, long cycling stability, economical price and environmental benignity has led to significant research interest in novel rechargeable batteries. In view of many restrictions encountered by LIBs, "non-lithium" secondary battery chemistry is one possible solution.

The main advantages of batteries based on non-lithium monovalent ions (SIBs and PIBs) is lower cost and more abundant resource of corresponding elements (Na and K) than Li. Recently, many novel electrode materials have been developed for SIBs. It is anticipated that SIBs will act as an appealing alternative to LIBs and potentially be used for hybrid electric vehicles and large-scale energy storage. However, there are many difficult problems to be solved, especially the lower volumetric energy density and the inferior cycling stability compared to LIBs. In contrast, the research interest in PIBs is relatively low due to the larger radius of K^+ and the inferior electrochemical performance to SIBs.

The multivalent ion batteries usually have a relatively high theoretical volumetric capacity and can avoid the formation of dendrites during charging, thus the safety issue originated from

the use of lithium or sodium metal anodes is prevented. The most significant problems to be resolved for high-performance multivalent ion batteries include the design of compatible electrolytes without side effects and the fabrication of high-voltage cathodes capable of transferring multiple electrons with rapid diffusion rate of the multivalent ions.

As highlighted throughout this review, the most critical aspects for the development of practically usable non-lithium rechargeable batteries are: (a) the discovery of novel electrode materials contributing to high energy density, rate capacity and cyclability; (b) the design of compatible electrolytes without side effects. The utilization of electrode materials with nano-/micro-scale hierarchical structured architectures will benefit solid-state diffusion of ions as well as structural integrity during intercalation/deintercalation but also may reduce the volumetric capacity of the electrodes. On the other hand, as one of the most important components in battery, electrolyte plays a crucial role for the electrochemical performances. Aqueous electrolyte usually has the advantages of good cyclability and low cost, but the limited ion concentration will inevitably restrict the further improvement of energy density. Many organic electrolytes are environmentally harmful, even though they have the possibility to provide relatively high capacity. Comparatively, ionic liquid electrolytes have shown a very good prospect, such as wide electrochemical window, environmentally benignity and high stability. However, electrolytes based on ionic liquids also have the disadvantages of high cost and large viscosity. Therefore, many aspects need to be taken into account in the pursuit of practical rechargeable non-lithium batteries. Undoubtedly, the research in this field is rapidly in development and certainly will bring actual advances in electrochemical energy storage.

Acknowledgments

This work is supported by the National Thousand Young Talents Program of China, the Young Scientists Project of National Basic Research Program of China (973 Program no. 2015CB659300), the National Natural Science Foundation of China (NSFC Grant nos. 21403105 and 21573108), the China Postdoctoral Science Foundation (Grant no. 2015M581768), the Natural Science Foundation for Young Scholars of Jiangsu Province (Grant nos. BK20150571 and BK20150583), the Fundamental Research Funds for the Central Universities and a project funded by the Priority Academic Program Development of Jiangsu Higher Education Institutions (PAPD).

References

[1] Chen K, Song S, Liu F, Xue D. Structural design of graphene for use in electrochemical energy storage devices. *Chem. Soc. Rev.* 2015;44:6230–6257.
[2] Zhao Y, Ding Y, Li Y, Peng L, Byon HR, Goodenough JB, Yu G. A chemistry and material perspective on lithium redox flow batteries towards high-density electrical energy storage. *Chem. Soc. Rev.* 2015;44:7968–7996.
[3] Mai L, Tian X, Xu X, Chang L, Xu L. Nanowire electrodes for electrochemical energy storage devices. *Chem. Rev.* 2014;114:11828–11862.
[4] Yabuuchi N, Kubota K, Dahbi M, Komaba S. Research development on sodium-ion batteries. *Chem. Rev.* 2014;114:11636–11682.
[5] Muldoon J, Bucur CB, Gregory T. Quest for nonaqueous multivalent secondary batteries: magnesium and beyond. *Chem. Rev.* 2014;114:11683–11720.
[6] Palacin MR. Recent advances in rechargeable battery materials: a chemist's perspective. *Chem. Soc. Rev.* 2009;38:2565–2575.
[7] Larcher D, Tarascon JM. Towards greener and more sustainable batteries for electrical energy storage. *Nat. Chem.* 2014;7:19–29.
[8] Zhou H, Wang Y, Li H, He P. The development of a new type of rechargeable batteries based on hybrid electrolytes. *ChemSusChem* 2010;3:1009–1019.
[9] Slater MD, Kim D, Lee E, Johnson CS. Sodium-ion batteries. *Adv. Funct. Mater.* 2013;23:947–958.
[10] Park M-S, Kim J-G, Kim Y-J, Choi N-S, Kim J-S. Recent advances in rechargeable magnesium battery technology: a review of the field's current status and prospects. *Isr. J. Chem.* 2015;55:570–585.
[11] Risacher F, Fritz B. Origin of salts and brine evolution of Bolivian and Chilean salars. *Aquat. Geochem.* 2009;15:123–157.
[12] Liu N, Lu Z, Zhao J, McDowell MT, Lee HW, Zhao W, Cui Y. A pomegranate-inspired nanoscale design for large-volume-change lithium battery anodes. *Nat. Nanotechnol.* 2014;9:187–192.
[13] Scrosati B, Hassoun J, Sun Y-K. Lithium-ion batteries. A look into the future. *Energy Environ. Sci.* 2011;4:3287–3295.
[14] Xu K. Nonaqueous liquid electrolytes for lithium-based rechargeable batteries. *Chem. Rev.* 2004;104:4303–4418.
[15] Zhou G, Paek E, Hwang GS, Manthiram A. Long-life Li/polysulphide batteries with high sulphur loading enabled by lightweight three-dimensional nitrogen/sulphur-codoped graphene sponge. *Nat. Commun.* 2015;6:7760–7770.
[16] Li F, Wu S, Li D, Zhang T, He P, Yamada A, Zhou H. The water catalysis at oxygen cathodes of lithium–oxygen cells. *Nat. Commun.* 2015;6:7843–7849.
[17] Xu C, Chen Y, Shi S, Li J, Kang F, Su D. Secondary batteries with multivalent ions for energy storage. *Sci. Rep.* 2015;5:14120–14124.
[18] Kundu D, Talaie E, Duffort V, Nazar LF. The emerging chemistry of sodium ion batteries for electrochemical energy storage. *Angew. Chem.* 2015;54:3431–3448.
[19] Wessells CD, Peddada SV, Huggins RA, Cui Y. Nickel hexacyanoferrate nanoparticle electrodes for aqueous sodium and potassium ion batteries. *Nano Lett.* 2011;11:5421–5425.
[20] Saha P, Datta MK, Velikokhatnyi OI, Manivannan A, Alman D, Kumta PN. Rechargeable magnesium battery: current status and key challenges for the future. *Prog. Mater. Sci.* 2014;66:1–86.
[21] Padigi P, Goncher G, Evans D, Solanki R. Potassium barium hexacyanoferrate-a potential cathode material for rechargeable calcium ion batteries. *J. Power Sources* 2015;273:460–464.
[22] Lin MC, Gong M, Lu B, Wu Y, Wang DY, Guan M, Angell M, Chen C, Yang J, Hwang BJ, Dai H. An ultrafast rechargeable aluminium-ion battery. *Nature* 2015;520:325–328.
[23] Alfaruqi MH, Mathew V, Gim J, Kim S, Song J, Baboo JP, Choi SH, Kim J. Electrochemically induced structural transformation in a γ-MnO_2 cathode of a high capacity zinc-ion battery system. *Chem. Mater.* 2015;27:3609–3620.
[24] Han MH, Gonzalo E, Singh G, Rojo T. A comprehensive review of sodium layered oxides: powerful cathodes for Na-ion batteries. *Energy Environ. Sci.* 2015;8:81–102.
[25] Komaba S, Hasegawa T, Dahbi M, Kubota K. Potassium intercalation into graphite to realize high-voltage/high-power potassium-ion batteries and potassium-ion capacitors. *Electrochem. Commun.* 2015;60:172–175.
[26] Sun J, Lee HW, Pasta M, Yuan H, Zheng G, Sun Y, Li Y, Cui Y. A phosphorene-graphene hybrid material as a high-capacity anode for sodium-ion batteries. *Nat. Nanotechnol.* 2015, http://dx.doi.org/10.1038/nnano.2015.1194.
[27] Rong Z, Malik R, Canepa P, Sai Gautam G, Liu M, Jain A, Persson K, Ceder G. Materials design rules for multivalent ion mobility in intercalation structures. *Chem. Mater.* 2015;27:6016–6021.
[28] Gautam GS, Canepa P, Malik R, Liu M, Persson K, Ceder G. First-principles evaluation of multi-valent cation insertion into orthorhombic V_2O_5. *Chem. Commun.* 2015;51:13619–13622.
[29] Xie J, Li C, Cui Z, Guo X. Transition-metal-free magnesium-based batteries activated by anionic insertion into fluorinated graphene nanosheets. *Adv. Funct. Mater.* 2015, http://dx.doi.org/10.1002/adfm.201503010.
[30] Li Z, Xiang K, Xing W, Carter WC, Chiang Y-M. Reversible aluminum-ion intercalation in Prussian blue analogs and demonstration of a high-power aluminum-ion asymmetric capacitor. *Adv. Energy Mater.* 2015;5:1401410–1401415.
[31] Molenda J, Delmas C, Hagenmuller P. Electronic and electrochemical properties of Na_xCoO_{2-y} cathode. *Solid State Ion.* 1983;9–10:431–435.
[32] Islam MS, Fisher CA. Lithium and sodium battery cathode materials: computational insights into voltage, diffusion and nanostructural properties. *Chem. Soc. Rev.* 2014;43:185–204.
[33] Kim S-W, Seo D-H, Ma X, Ceder G, Kang K. Electrode materials for rechargeable sodium-ion batteries:potential alternatives to current lithium-ion batteries. *Adv. Energy Mater.* 2012;2:710–721.
[34] Pan H, Hu Y-S, Chen L. Room-temperature stationary sodium-ion batteries for large-scale electric energy storage. *Energy Environ. Sci.* 2013;6:2338–2360.
[35] Wu L, Hu XH, Qian JF, Pei F, Wu FY, Mao RJ, Ai XP, Yang HX, Cao YL. Sb–C nanofibers with long cycle life as an anode material for high-performance sodium-ion batteries. *Energy Environ. Sci.* 2014;7:323–328.
[36] Hamani D, Ati M, Tarascon J-M, Rozier P. Na_xVO_2 as possible electrode for Na-ion batteries. *Electrochem. Commun.* 2011;13:938–941.
[37] Komaba S, Takei C, Nakayama T, Ogata A, Yabuuchi N. Electrochemical intercalation activity of layered $NaCrO_2$ vs. $LiCrO_2$. *Electrochem. Commun.* 2010;12:355–358.
[38] Mendiboure A, Delmas C, Hagenmuller P. Electrochemical intercalation and deintercalation of Na_xMnO_2 bronzes. *J. Solid State Chem.* 1985;57:323–331.
[39] Takeda Y, Nakahara K, Nishijima M, Imanishi N, Yamamoto O, Takano M, Kanno R. Sodium deintercalation from sodium iron oxide. *Mater. Res. Bull.* 1994;29:659–666.
[40] Ding JJ, Zhou YN, Sun Q, Yu XQ, Yang XQ, Fu ZW. Electrochemical properties of P2-phase $Na_{0.74}CoO_2$ compounds as cathode material for rechargeable sodium-ion batteries. *Electrochim. Acta* 2013;87:388–393.

[41] Yabuuchi N, Yano M, Yoshida H, Kuze S, Komaba S. Synthesis and electrode performance of O3-Type $NaFeO_2$-$NaNi_{1/2}Mn_{1/2}O_2$ solid solution for rechargeable sodium batteries. *J. Electrochem. Soc.* 2013;160:A3131–A3137.

[42] Yu C-Y, Park J-S, Jung H-G, Chung K-Y, Aurbach D, Sun Y-K, Myung S-T. $NaCrO_2$ cathode for high rate sodium-ion batteries. *Energy Environ. Sci.* 2015;8:2019–2026.

[43] Wang XF, Gao YR, Shen X, Li YJ, Kong QY, Lee SS, Wang ZX, Yu R, Hu YS, Chen LQ. Anti-P-2 structured $Na_{0.5}NbO_2$ and its negative strain effect. *Energy Environ. Sci.* 2015;8:2753–2759.

[44] Dong Y, Li S, Zhao K, Han C, Chen W, Wang B, Wang L, Xu B, Wei Q, Zhang L, Xu X, Mai L. Hierarchical zigzag $Na_{1.25}V_3O_8$ nanowires with topotactically encoded superior performance for sodium-ion battery cathodes. *Energy Environ. Sci.* 2015;8:1267–1275.

[45] Sau K, Kumar PP. Role of ion–ion correlations on fast ion transport: molecular dynamics simulation of $Na_2Ni_2TeO_6$. *J. Phys. Chem. C* 2015;119:18030–18037.

[46] Yu H, Guo S, Zhu Y, Ishida M, Zhou H. Novel titanium-based O3-type $NaTi_{0.5}Ni_{0.5}O_2$ as a cathode material for sodium ion batteries. *Chem. Commun.* 2014;50:457–459.

[47] Ma J, Bo S-H, Wu L, Zhu Y, Grey CP, Khalifah PG. Ordered and disordered polymorphs of $Na(Ni_{2/3}Sb_{1/3})O_2$: honeycomb-ordered cathodes for Na-ion batteries. *Chem. Mater.* 2015;27:2387–2399.

[48] Sun X, Jin Y, Zhang C-Y, Wen J-W, Shao Y, Zang Y, Chen C-H. $Na[Ni_{0.4}Fe_{0.2}Mn_{0.4-x}Ti_x]O_2$: a cathode of high capacity and superior cyclability for Na-ion batteries. *J. Mater. Chem. A* 2014;2:17268–17271.

[49] Xu S, Wang Y, Ben L, Lyu Y, Song N, Yang Z, Li Y, Mu L, Yang H-T, Gu L, Hu Y-S, Li X, Cheng Z-H, Chen L, Huang X. Fe-based tunnel-type $Na_{0.61}[Mn_{0.27}Fe_{0.34}Ti_{0.39}]O_2$ designed by a new strategy as a cathode material for sodium-ion batteries. *Adv. Energy Mater.* 2015:1501156–1502264.

[50] Sathiya M, Hemalatha K, Ramesha K, Tarascon JM, Prakash AS. Synthesis, structure, and electrochemical properties of the layered sodium insertion cathode material: $NaNi_{1/3}Mn_{1/3}Co_{1/3}O_2$. *Chem. Mater.* 2012;24:1846–1853.

[51] Yuan D, He W, Pei F, Wu F, Wu Y, Qian J, Cao Y, Ai X, Yang H. Synthesis and electrochemical behaviors of layered $Na_{0.67}[Mn_{0.65}Co_{0.2}Ni_{0.15}]O_2$ microflakes as a stable cathode material for sodium-ion batteries. *J. Mater. Chem. A* 2013;1:3895–3899.

[52] Lu Y, Yanilmaz M, Chen C, Ge Y, Dirican M, Zhu J, Li Y, Zhang X. Lithium-substituted sodium layered transition metal oxide fibers as cathodes for sodium-ion batteries. *Energy Storage Mater.* 2015;1:74–81.

[53] Hwang J-Y, Oh S-M, Myung S-T, Chung KY, Belharouak I, Sun Y-K. Radially aligned hierarchical columnar structure as a cathode material for high energy density sodium-ion batteries. *Nat. Commun.* 2015;6:6865–6872.

[54] Ferlay S, Mallah T, Ouahes R, Veillet P, Verdaguer M. A room-temperature organometallic magnet based on Prussian blue. *Nature* 1995;378:701–703.

[55] Wang L, Lu Y, Liu J, Xu M, Cheng J, Zhang D, Goodenough JB. A superior low-cost cathode for a Na-ion battery. *Angew. Chem. Int. Ed.* 2013;52:1964–1967.

[56] Robin MB. The color and electronic configurations of Prussian blue. *Inorg. Chem.* 1962;1:337–342.

[57] Scholz F, Dostal A. The formal potentials of solid metal hexacyanometalates. *Angew. Chem. Int. Ed. Engl.* 1996;34:2685–2687.

[58] Wang RY, Wessells CD, Huggins RA, Cui Y. Highly reversible open framework nanoscale electrodes for divalent ion batteries. *Nano Lett.* 2013;13:5748–5752.

[59] Pasta M, Wessells CD, Liu N, Nelson J, McDowell MT, Huggins RA, Toney MF, Cui Y. Full open-framework batteries for stationary energy storage. *Nat. Commun.* 2014;5:3007–3015.

[60] You Y, Wu X-L, Yin Y-X, Guo Y-G. High-quality Prussian blue crystals as superior cathode materials for room-temperature sodium-ion batteries. *Energy Environ. Sci.* 2014;7:1643–1647.

[61] Lee HW, Wang RY, Pasta M, Woo Lee S, Liu N, Cui Y. Manganese hexacyanomanganate open framework as a high-capacity positive electrode material for sodium-ion batteries. *Nat. Commun.* 2014;5:5280–5285.

[62] Liu Y, Qiao Y, Zhang W, Li Z, Ji X, Miao L, Yuan L, Hu X, Huang Y. Sodium storage in Na-rich $Na_xFeFe(CN)_6$ nanocubes. *Nano Energy* 2015;12:386–393.

[63] Lee KT, Ramesh T, Nan F, Botton G, Nazar LF. Topochemical synthesis of sodium metal phosphate olivines for sodium-ion batteries. *Chem. Mater.* 2011;23:3593–3600.

[64] Casas-Cabanas M, Roddatis VV, Saurel D, Kubiak P, Carretero-González J, Palomares T, Serras P, Rojo T. Crystal chemistry of Na insertion/deinsertion in $FePO_4$-$NaFePO_4$. *J. Mater. Chem.* 2012;22:17421–17423.

[65] Oh S-M, Myung S-T, Hassoun J, Scrosati B, Sun Y-K. Reversible $NaFePO_4$ electrode for sodium secondary batteries. *Electrochem. Commun.* 2012;22:149–152.

[66] Kim J, Seo D-H, Kim H, Park I, Yoo J-K, Jung S-K, Park Y-U, Goddard Iii WA, Kang K. Unexpected discovery of low-cost maricite $NaFePO_4$ as a high-performance electrode for Na-ion batteries. *Energy Environ. Sci.* 2015;8:540–545.

[67] Li C, Miao X, Chu W, Wu P, Tong DG. Hollow amorphous NaFePO4nanospheres as a high-capacity and high-rate cathode for sodium-ion batteries. *J. Mater. Chem. A* 2015;3:8265–8271.

[68] Saravanan K, Mason CW, Rudola A, Wong KH, Balaya P. The first report on excellent cycling stability and superior rate capability of $Na_3V_2(PO_4)_3$ for sodium ion batteries. *Adv. Energy Mater.* 2013;3:444–450.

[69] Zhu C, Song K, van Aken PA, Maier J, Yu Y. Carbon-coated $Na_3V_2(PO_4)_3$ embedded in porous carbon matrix: an ultrafast Na-storage cathode with the potential of outperforming Li cathodes. *Nano Lett.* 2014;14:2175–2180.

[70] Li S, Dong Y, Xu L, Xu X, He L, Mai L. Effect of carbon matrix dimensions on the electrochemical properties of $Na_3V_2(PO_4)_3$ nanograins for high-performance symmetric sodium-ion batteries. *Adv. Mater.* 2014;26:3545–3553.

[71] Liu J, Tang K, Song K, van Aken PA, Yu Y, Maier J. Electrospun $Na_3V_2(PO_4)_3$/C nanofibers as stable cathode materials for sodium-ion batteries. *Nanoscale* 2014;6:5081–5086.

[72] Fang Y, Xiao L, Ai X, Cao Y, Yang H. Hierarchical carbon framework wrapped $Na_3V_2(PO_4)_3$ as a superior high-rate and extended lifespan cathode for sodium-ion batteries. *Adv. Mater.* 2015;27:5895–5900.

[73] Shakoor RA, Seo D-H, Kim H, Park Y-U, Kim J, Kim S-W, Gwon H, Lee S, Kang K. A combined first principles and experimental study on $Na_3V_2(PO_4)_2F_3$ for rechargeable Na batteries. *J. Mater. Chem.* 2012;22:20535–20541.

[74] Bianchini M, Fauth F, Brisset N, Weill F, Suard E, Masquelier C, Croguennec L. Comprehensive investigation of the $Na_3V_2(PO_4)_2F_3$-$NaV_2(PO_4)_2F_3$ system by operando high resolution synchrotron X-ray diffraction. *Chem. Mater.* 2015;27:3009–3020.

[75] Park YU, Seo DH, Kwon HS, Kim B, Kim J, Kim H, Kim I, Yoo HI, Kang K. A new high-energy cathode for a Na-ion battery with ultrahigh stability. *J. Am. Chem. Soc.* 2013;135:13870–13878.

[76] Barpanda P, Nishimura S-i, Yamada A. High-voltage pyrophosphate cathodes. *Adv. Energy Mater.* 2012;2:841–859.

[77] Barpanda P, Liu G, Ling CD, Tamaru M, Avdeev M, Chung S-C, Yamada Y, Yamada A. $Na_2FeP_2O_7$: a safe cathode for rechargeable sodium-ion batteries. *Chem. Mater.* 2013;25:3480–3487.

[78] Barpanda P, Avdeev M, Ling CD, Lu J, Yamada A. Magnetic structure and properties of the $Na_2CoP_2O_7$ pyrophosphate cathode for sodium-ion batteries: a supersuperexchange-driven non-collinear antiferromagnet. *Inorg. Chem.* 2013;52:395–401.

[79] Park CS, Kim H, Shakoor RA, Yang E, Lim SY, Kahraman R, Jung Y, Choi JW. Anomalous manganese activation of a pyrophosphate cathode in sodium ion batteries: a combined experimental and theoretical study. *J. Am. Chem. Soc.* 2013;135:2787–2792.

[80] Nose M, Nakayama H, Nobuhara K, Yamaguchi H, Nakanishi S, Iba H. $Na_4Co_3(PO_4)_2P_2O_7$: a novel storage material for sodium-ion batteries. *J. Power Sources* 2013;234:175–179.

[81] Nose M, Shiotani S, Nakayama H, Nobuhara K, Nakanishi S, Iba H. $Na_4Co_{2.4}Mn_{0.3}Ni_{0.3}(PO_4)_2P_2O_7$: high potential and high capacity electrode material for sodium-ion batteries. *Electrochem. Commun.* 2013;34:266–269.

[82] Reynaud M, Rousse G, Abakumov AM, Sougrati MT, Van Tendeloo G, Chotard J-N, Tarascon J-M. Design of new electrode materials for Li-ion and Na-ion batteries from the bloedite mineral $Na_2Mg(SO_4)_2 \cdot 4H_2O$. *J. Mater. Chem. A* 2014;2:2671–2680.

[83] Barpanda P, Oyama G, Ling CD, Yamada A. Kröhnkite-Type $Na_2Fe(SO_4)_2 \cdot 2H_2O$ as a novel 3.25 V insertion compound for Na-Ion batteries. *Chem. Mater.* 2014;26:1297–1299.

[84] Barpanda P, Oyama G, Nishimura S-i, Chung S-C, Yamada A. A 3.8-V earth-abundant sodium battery electrode. *Nat. Commun.* 2014;5:4358–4365.

[85] Wen Y, He K, Zhu Y, Han F, Xu Y, Matsuda I, Ishii Y, Cumings J, Wang C. Expanded graphite as superior anode for sodium-ion batteries. *Nat. Commun.* 2014;5:4033–4042.

[86] Stevens DA, Dahn JR. The mechanisms of lithium and sodium insertion in carbon materials. *J. Electrochem. Soc.* 2001;148:A803–A811.

[87] Wang Y-X, Chou S-L, Liu H-K, Dou S-X. Reduced graphene oxide with superior cycling stability and rate capability for sodium storage. *Carbon* 2013;57:202–208.

[88] Cao Y, Xiao L, Sushko ML, Wang W, Schwenzer B, Xiao J, Nie Z, Saraf LV, Yang Z, Liu J. Sodium ion insertion in hollow carbon nanowires for battery applications. *Nano Lett.* 2012;12:3783–3787.

[89] Tang K, Fu L, White RJ, Yu L, Titirici M-M, Antonietti M, Maier J. Hollow carbon nanospheres with superior rate capability for sodium-based batteries. *Adv. Energy Mater.* 2012;2:873–877.

[90] Stevensa JRDDA. High capacity anode materials for rechargeable sodium-ion batteries. *J. Electrochem. Soc.* 2000;147:1271–1273.

[91] Wenzel S, Hara T, Janek J, Adelhelm P. Room-temperature sodium-ion batteries: Improving the rate capability of carbon anode materials by templating strategies. *Energy Environ. Sci.* 2011;4:3342–3345.

[92] Jache B, Adelhelm P. Use of graphite as a highly reversible electrode with superior cycle life for sodium-ion batteries by making use of co-intercalation phenomena. *Angew. Chem.* 2014;53:10169–10173.

[93] Zhang J, Lv W, Tao Y, He Y-B, Wang D-W, You C-H, Li B, Kang F, Yang Q-H. Ultrafast high-volumetric sodium storage of folded-graphene electrodes through surface-induced redox reactions. *Energy Storage Mater.* 2015;1:112–118.

[94] Jian Z, Xing Z, Bommier C, Li Z, Ji X. Hard carbon microspheres: potassium-ion anode versus sodium-ion anode. *Adv. Energy Mater.* 2015, http://dx.doi.org/10.1002/aenm.201501874.

[95] Kim H, Hong J, Park Y-U, Kim J, Hwang I, Kang K. Sodium storage behavior in natural graphite using ether-based electrolyte systems. *Adv. Funct. Mater.* 2015;25:534–541.

[96] Zhang S-W, Lv W, Luo C, You C-H, Zhang J, Pan Z-Z, Kang F-Y, Yang Q-H. Commercial carbon molecular sieves as a high performance anode for sodium-ion batteries. *Energy Storage Mater.* 2016;3:18–23.

[97] Ge P, Fouletier M. Electrochemical intercalation of sodium in graphite. *Solid State Ion.* 1988;28–30:1172–1175.

[98] Li Y, Mu L, Hu Y-S, Li H, Chen L, Huang X. Pitch-derived amorphous carbon as high performance anode for sodium-ion batteries. *Energy Storage Mater.* 2016;2:139–145.

[99] Qian J, Wu X, Cao Y, Ai X, Yang H. High capacity and rate capability of amorphous phosphorus for sodium ion batteries. *Angew. Chem.* 2013;52:4633–4636.

[100] Kim Y, Park Y, Choi A, Choi NS, Kim J, Lee J, Ryu JH, Oh SM, Lee KT. An amorphous red phosphorus/carbon composite as a promising anode material for sodium ion batteries. *Adv. Mater.* 2013;25:3045–3049.

[101] Song J, Yu Z, Gordin ML, Hu S, Yi R, Tang D, Walter T, Regula M, Choi D, Li X, Manivannan A, Wang D. Chemically bonded phosphorus/graphene hybrid as a high performance anode for sodium-ion batteries. *Nano Lett.* 2014;14:6329–6335.

[102] Zhu Y, Wen Y, Fan X, Gao T, Han F, Luo C, Liou S-C, Wang C. Red phosphorus–single-walled carbon nanotube composite as a superior anode for sodium ion batteries. *ACS Nano* 2015;9:3254–3264.

[103] Li WJ, Chou SL, Wang JZ, Liu HK, Dou SX. Simply mixed commercial red phosphorus and carbon nanotube composite with exceptionally reversible sodium-ion storage. *Nano Lett.* 2013;13:5480–5484.

[104] Li WJ, Chou SL, Wang JZ, Liu HK, Dou SX. A new, cheap, and productive FeP anode material for sodium-ion batteries. *Chem. Commun.* 2015;51:3682–3685.

[105] Fullenwarth J, Darwiche A, Soares A, Donnadieu B, Monconduit L. NiP_3: a promising negative electrode for Li- and Na-ion batteries. *J. Mater. Chem. A* 2014;2:2050–2059.

[106] Fan X, Mao J, Zhu Y, Luo C, Suo L, Gao T, Han F, Liou S-C, Wang C. Superior stable self-healing SnP_3 anode for sodium-ion batteries. *Adv. Energy Mater.* 2015:1500174–1500180.

[107] Qian J, Xiong Y, Cao Y, Ai X, Yang H. Synergistic Na-storage reactions in Sn_4P_3 as a high-capacity, cycle-stable anode of Na-ion batteries. *Nano Lett.* 2014;14:1865–1869.

[108] Kim Y, Kim Y, Choi A, Woo S, Mok D, Choi NS, Jung YS, Ryu JH, Oh SM, Lee KT. Tin phosphide as a promising anode material for Na-ion batteries. *Adv. Mater.* 2014;26:4139–4144.

[109] Xu Y, Zhu Y, Liu Y, Wang C. Electrochemical performance of porous carbon/tin composite anodes for sodium-ion and lithium-ion batteries. *Adv. Energy Mater.* 2013;3:128–133.

[110] Farbod B, Cui K, Kalisvaart WP, Kupsta M, Zahiri B, Kohandehghan A, Lotfabad EM, Li Z, Luber EJ, Mitlin. D. Anodes for sodium ion batteries based on tin-germanium-antimony Alloys. *ACS Nano* 2014;8:4415–4429.

[111] Kim Y, Ha KH, Oh SM, Lee KT. High-capacity anode materials for sodium-ion batteries. *Chemistry* 2014;20:11980–11992.

[112] He M, Kravchyk K, Walter M, Kovalenko MV. Monodisperse antimony nanocrystals for high-rate Li-ion and Na-ion battery anodes: nano versus bulk. *Nano Lett.* 2014;14:1255–1262.

[113] Liu J, Yang Z, Wang J, Gu L, Maier J, Yu Y. Three-dimensionally interconnected nickel-antimony intermetallic hollow nanospheres as anode material for high-rate sodium-ion batteries. *Nano Energy* 2015;16:389–398.

[114] Xie X, Kretschmer K, Zhang J, Sun B, Su D, Wang G. Sn@CNT nanopillars grown perpendicularly on carbon paper: A novel free-standing anode for sodium ion batteries. *Nano Energy* 2015;13:208–217.

[115] Zhao Y, Manthiram A. High-capacity, high-rate Bi–Sb alloy anodes for lithium-ion and sodium-ion batteries. *Chem. Mater.* 2015;27:3096–3101.

[116] Xiao L, Cao Y, Xiao J, Wang W, Kovarik L, Nie Z, Liu J. High capacity, reversible alloying reactions in SnSb/C nanocomposites for Na-ion battery applications. *Chem. Commun.* 2012;48:3321–3323.

[117] Liu Y, Zhang N, Jiao L, Tao Z, Chen J. Ultrasmall Sn nanoparticles embedded in carbon as high-performance anode for sodium-ion batteries. *Adv. Funct. Mater.* 2015;25:214–220.

[118] Senguttuvan P, Rousse G, Seznec V, Tarascon J-M, Palacín MR. $Na_2Ti_3O_7$: lowest voltage ever reported oxide insertion electrode for sodium ion batteries. *Chem. Mater.* 2011;23:4109–4111.

[119] Wu D, Li X, Xu B, Twu N, Liu L, Ceder G. $NaTiO_2$: a layered anode material for sodium-ion batteries. *Energy Environ. Sci.* 2015;8:195–202.

[120] Wang Y, Yu X, Xu S, Bai J, Xiao R, Hu YS, Li H, Yang XQ, Chen L, Huang X. A zero-strain layered metal oxide as the negative electrode for long-life sodium-ion batteries. *Nat. Commun.* 2013;4:2365–2371.

[121] Park SI, Gocheva I, Okada S, Yamaki J-i. Electrochemical properties of $NaTi_2(PO_4)_3$ anode for rechargeable aqueous sodium-ion batteries. *J. Electrochem. Soc.* 2011;158:A1067–A1070.

[122] Wang Y, Liu J, Lee B, Qiao R, Yang Z, Xu S, Yu X, Gu L, Hu YS, Yang W, Kang K, Li H, Yang XQ, Chen L, Huang X. Ti-substituted tunnel-type $Na_{0.44}MnO_2$ oxide as a negative electrode for aqueous sodium-ion batteries. *Nat. Commun.* 2015;6:6401–6410.

[123] Zhang N, Han X, Liu Y, Hu X, Zhao Q, Chen J. 3D Porous γ-Fe_2O_3@C nanocomposite as high-performance anode material of Na-ion batteries. *Adv. Energy Mater.* 2015;5:1401123–1401129.

[124] Yuan S, Huang XL, Ma DL, Wang HG, Meng FZ, Zhang XB. Engraving copper foil to give large-scale binder-free porous CuO arrays for a high-performance sodium-ion battery anode. *Adv. Mater.* 2014;26:2273–2279.

[125] Schaub R, Wahlström E, Rønnau A, Lægsgaard E, Stensgaard I, Besenbacher F. Oxygen-mediated diffusion of oxygen vacancies on the TiO_2 (110) surface. *Science* 2003;299:377–379.

[126] Hariharan S, Saravanan K, Balaya P. α-MoO_3: a high performance anode material for sodium-ion batteries. *Electrochem. Commun.* 2013;31:5–9.

[127] Xu Y, Zhou M, Wang X, Wang C, Liang L, Grote F, Wu M, Mi Y, Lei Y. Enhancement of sodium ion battery performance enabled by oxygen vacancies. *Angew. Chem.* 2015;54:1–5.

[128] Hu Z, Zhu Z, Cheng F, Zhang K, Wang J, Chen C, Chen J. Pyrite FeS_2 for high-rate and long-life rechargeable sodium batteries. *Energy Environ. Sci.* 2015;8:1309–1316.

[129] Wang J, Luo C, Gao T, Langrock A, Mignerey AC, Wang C. An advanced MoS_2/carbon anode for high-performance sodium-ion batteries. *Small* 2015;11:473–481.

[130] Zhang SS. The redox mechanism of FeS_2 in non-aqueous electrolytes for lithium and sodium batteries. *J. Mater. Chem. A* 2015;3:7689–7694.

[131] Walter M, Zund T, Kovalenko MV. Pyrite (FeS_2) nanocrystals as inexpensive high-performance lithium-ion cathode and sodium-ion anode materials. *Nanoscale* 2015;7:9158–9163.

[132] Wang X, Li Y, Guan Z, Wang Z, Chen L. Micro-MoS_2 with excellent reversible sodium-ion storage. *Chemistry* 2015;21:6465–6468.

[133] Hu Z, Wang L, Zhang K, Wang J, Cheng F, Tao Z, Chen J. MoS_2 nanoflowers with expanded interlayers as high-performance anodes for sodium-ion batteries. *Angew. Chem.* 2014;126:13008–13012.

[134] Ko YN, Choi SH, Park SB, Kang YC. Hierarchical $MoSe_2$ yolk-shell microspheres with superior Na-ion storage properties. *Nanoscale* 2014;6:10511–10515.

[135] Zhang K, Hu Z, Liu X, Tao Z, Chen J. $FeSe_2$ Microspheres as a high-performance anode material for Na-ion batteries. *Adv. Mater.* 2015;27:3305–3309.

[136] Eftekhari A. Potassium secondary cell based on Prussian blue cathode. *J. Power Sources* 2004;126:221–228.

[137] Nishizawa M, Uchiyama T, Dokko K, Yamada K, Matsue T, Uchida I. Electrochemical studies of spinel $LiMn_2O_4$ films prepared by electrostatic spray deposition. *Bull. Chem. Soc. Jpn.* 1998;71:2011–2015.

[138] Wessells CD, Huggins RA, Cui Y. Copper hexacyanoferrate battery electrodes with long cycle life and high power. *Nat. Commun.* 2011;2:550–554.

[139] Padigi P, Thiebes J, Swan M, Goncher G, Evans D, Solanki R. Prussian green: a high rate capacity cathode for potassium ion batteries. *Electrochim. Acta* 2015;166:32–39.

[140] Luo W, Wan J, Ozdemir B, Bao W, Chen Y, Dai J, Lin H, Xu Y, Gu F, Barone V, Hu L. Potassium ion batteries with graphitic materials. *Nano Lett.* 2015;15:7671–7677.

[141] Matsui M. Study on electrochemically deposited Mg metal. *J. Power Sources* 2011;196:7048–7055.

[142] Aurbach ZLD, Schechter A, Gofer Y, Gizbar H, Turgeman R, Cohen Y, Moshkovich M, Levi E. Prototype systems for rechargeable magnesium batteries. *Nature* 2000;407:724–727.

[143] Huie MM, Bock DC, Takeuchi ES, Marschilok AC, Takeuchi KJ. Cathode materials for magnesium and magnesium-ion based batteries. *Coord. Chem. Rev.* 2015;287:15–27.

[144] Levi E, Mitelman A, Aurbach D, Brunelli M. Structural mechanism of the phase transitions in the $Mg-Cu-Mo_6S_8$ system probed by ex situ synchrotron X-ray diffraction. *Chem. Mater.* 2007;19:5131–5142.

[145] Levi E, Gershinsky G, Aurbach D, Isnard O. Crystallography of chevrel phases, MMo_6T_8 (M=Cd, Na, Mn, and Zn, T=S, Se) and their cation mobility. *Inorg. Chem.* 2009;48:8751–8758.

[146] Levi E, Aurbach D. Chevrel Phases, $M_xMo_6T_8$ (M=Metals, T=S, Se, Te) as a structural chameleon: changes in the rhombohedral framework and triclinic distortion. *Chem. Mater.* 2010;22:3678–3692.

[147] Chusid O, Gofer Y, Gizbar H, Vestfrid Y, Levi E, Aurbach D, Riech I. solid-state rechargeable magnesium battery. *Adv. Mater.* 2003;15:627–630.

[148] Aurbach D, Suresh GS, Levi E, Mitelman A, Mizrahi O, Chusid O, Brunelli M. Progress in rechargeable magnesium battery technology. *Adv. Mater.* 2007;19:4260–4267.

[149] Enjalbert R, Galy J. A refinement of the structure of V_2O_5. *Acta Crystallogr. Sect. C: Cryst. Struct. Commun.* 1986;42:1467–1469.

[150] Petr Nov6k JD. Electrochemical insertion of magnesium in metal oxides and sulfides from aprotic electrolytes. *J. Electrochem. Soc.* 1993;140:140–144.

[151] Novak RIP, Haas O. Magnesium insertion electrodes for rechargeable nonaqueous battery-a competitive lithium.pdf. *Electrochim. Acta* 1999;45:351–367.

[152] Amatucci GG, Badway F, Singhal A, Beaudoin B, Skandan G, Bowmer T, Plitz I, Pereira N, Chapman T, Jaworski R. Investigation of yttrium and polyvalent ion intercalation into nanocrystalline vanadium oxide. *J. Electrochem. Soc.* 2001;148:A940–A950.

[153] Jiao L, Yuan H, Si Y, Wang Y, Cao J, Gao X, Zhao M, Zhou X, Wang Y. Electrochemical insertion of magnesium in open-ended vanadium oxide nanotubes. *J. Power Sources* 2006;156:673–676.

[154] Jiao L, Yuan H, Wang Y, Cao J, Wang Y. Mg intercalation properties into open-ended vanadium oxide nanotubes. *Electrochem. Commun.* 2005;7:431–436.

[155] Jiao L-F, Yuan H-T, Si Y-C, Wang Y-J, Wang Y-M. Synthesis of $Cu_{0.1}$-doped vanadium oxide nanotubes and their application as cathode materials for rechargeable magnesium batteries. *Electrochem. Commun.* 2006;8:1041–1044.

[156] Imamura D. Characterization of magnesium-intercalated V_2O_5/carbon composites. *Solid State Ion.* 2003;161:173–180.

[157] Imamura D, Miyayama M, Hibino M, Kudo T. Mg intercalation properties into V_2O_5 gel/Carbon composites under high-rate condition. *J. Electrochem. Soc.* 2003;150:A753–A758.

[158] Okoshi M, Yamada Y, Yamada A, Nakai H. Theoretical analysis on de-solvation of lithium, sodium, and magnesium cations to organic electrolyte solvents. *J. Electrochem. Soc.* 2013;160:A2160–A2165.

[159] Miura H. The crystal structure of hollandite. *Mineral. J.* 1986;13:119–129.
[160] Post DLBJE. Rietveld refinement of the todorokite structure. *Am. Mineral.* 1988;73:861–869.
[161] Post DRVJE. Crystal structure determinations of synthetic sodium, magnesium, and potassium brinessite using TEM and the Rietveld method. *Am. Mineral.* 1990;75:477–489.
[162] Fong C, Kennedy B, Elcombe M. A powder neutron diffraction study of λ and γ manganese dioxide and of $LiMn_2O_4$. *Z. Krist.* 1994;209:941–945.
[163] Zhang R, Yu X, Nam K-W, Ling C, Arthur TS, Song W, Knapp AM, Ehrlich SN, Yang X-Q, Matsui M. α-MnO_2 as a cathode material for rechargeable Mg batteries. *Electrochem. Commun.* 2012;23:110–113.
[164] Yuan C, Zhang Y, Pan Y, Liu X, Wang G, Cao D. Investigation of the intercalation of polyvalent cations (Mg^{2+}, Zn^{2+}) into λ-MnO_2 for rechargeable aqueous battery. *Electrochim. Acta* 2014;116:404–412.
[165] Tenne R. Advances in the synthesis of inorganic nanotubes and fullerene-like nanoparticles. *Angew. Chem.* 2003;42:5124–5132.
[166] Xiao J, Choi D, Cosimbescu L, Koech P, Liu J, Lemmon JP. Exfoliated MoS_2 nanocomposite as an anode material for lithium ion batteries. *Chem. Mater.* 2010;22:4522–4524.
[167] Bell RE, Herfert RE. Preparation and characterization of a new crystalline form of molybdenum disulfide. *J. Am. Chem. Soc.* 1957;79:3351–3354.
[168] Li X-L, Li Y-D. MoS2 Nanostructures: synthesis and electrochemical Mg^{2+}intercalation. *J. Phys. Chem. B* 2004;108:13893–13900.
[169] Liang YL, Feng RJ, Yang SQ, Ma H, Liang J, Chen J. Rechargeable Mg batteries with graphene-like MoS_2 cathode and ultrasmall Mg nanoparticle anode. *Adv. Mater.* 2011;23:640–643.
[170] Chiritescu Catalin, Cahill David G, Nguyen Ngoc, Johnson David, Bodapati Arun, Keblinski Pawel, Zschack P. Atmospheric pressure chemical vapor deposition of WSe_2 thin films on glass; highly hydrophobic sticky surfaces. *Science* 2007;315:351–353.
[171] Boscher ND, Carmalt CJ, Parkin IP. Atmospheric pressure chemical vapor deposition of WSe_2 thin films on glass-highly hydrophobic sticky surfaces. *J. Mater. Chem.* 2006;16:122–127.
[172] Fang H, Chuang S, Chang TC, Takei K, Takahashi T, Javey A. High-performance single layered WSe_2 p-FETs with chemically doped contacts. *Nano Lett.* 2012;12:3788–3792.
[173] Liu B, Luo T, Mu G, Wang X, Chen D, Shen G. Rechargeable Mg-ion batteries based on WSe_2 nanowire cathodes. *ACS Nano* 2013;7:8051–8058.
[174] Tao ZL, Xu LN, Gou XL, Chen J, Yuan HT. TiS_2 nanotubes as the cathode materials of Mg-ion batteries. *Chem. Commun.* 2004:2080–2081.
[175] Peng B, Chen J. Functional materials with high-efficiency energy storage and conversion for batteries and fuel cells. *Coord. Chem. Rev.* 2009;253:2805–2813.
[176] Li W, Li C, Zhou C, Ma H, Chen J. Metallic magnesium nano/mesoscale structures: their shape-controlled preparation and Mg/air battery applications. *Angew. Chem.* 2006;118:6155–6158.
[177] Yoo HD, Shterenberg I, Gofer Y, Gershinsky G, Pour N, Aurbach D. Mg rechargeable batteries: an on-going challenge. *Energy Environ. Sci.* 2013;6:2265–2279.
[178] Muldoon John, Bucur Claudiu B, Oliver Allen G, Sugimoto Tsuyoshi, Matsui Masaki, Kim Hee Soo, Allred Gary D, Zajicekb Jaroslav, Kotani Y. Electrolyte roadblocks to a magnesium rechargeable battery. *Energy Environ. Sci.* 2012;5:5941–5950.
[179] Arthur TS, Singh N, Matsui M. Electrodeposited Bi, Sb and $Bi_{1-x}Sb_x$ alloys as anodes for Mg-ion batteries. *Electrochem. Commun.* 2012;16:103–106.
[180] Watson L, Marshall C, Cardoso C. On the electronic structure of the semiconducting compounds Mg_3Bi_2 and Mg_3Sb_2. *J. Phys. F: Met. Phys.* 1984;14:113–121.
[181] Poizot P, Laruelle S, Grugeon S, Dupont L, Tarascon J-M. Nano-sized transition-metaloxides as negative-electrode materials for lithium-ion battery. *Nature* 2000;407:496–499.
[182] Amine K, Belharouak I, Chen Z, Tran T, Yumoto H, Ota N, Myung ST, Sun YK. Nanostructured anode material for high-power battery system in electric vehicles. *Adv. Mater.* 2010;22:3052–3057.
[183] Shao Y, Gu M, Li X, Nie Z, Zuo P, Li G, Liu T, Xiao J, Cheng Y, Wang C, Zhang JG, Liu J. Highly reversible Mg insertion in nanostructured Bi for Mg ion batteries. *Nano Lett.* 2014;14:255–260.
[184] Singh N, Arthur TS, Ling C, Matsui M, Mizuno F. A high energy-density tin anode for rechargeable magnesium-ion batteries. *Chem. Commun.* 2013;49:149–151.
[185] Wang Z, Su Q, Shi J, Deng H, Yin GQ, Guan J, Wu MP, Zhou YL, Lou HL, Fu YQ. Comparison of tetragonal and cubic tin as anode for Mg ion batteries. *ACS Appl. Mater. Interfaces* 2014;6:6786–6789.
[186] Wu N, Lyu Y-C, Xiao R-J, Yu X, Yin Y-X, Yang X-Q, Li H, Gu L, Guo Y-G. A highly reversible, low-strain Mg-ion insertion anode material for rechargeable Mg-ion batteries. *NPG Asia Mater.* 2014;6:e120–e126.
[187] Levi E, Gofer Y, Aurbach D. On the way to rechargeable Mg batteries: the challenge of new cathode materials. *Chem. Mater.* 2010;22:860–868.
[188] Aurbach D, Skaletsky R, Gofer Y. The electrochemical behavior of calcium electrodes in a few organic electrolytes. *J. Electrochem. Soc.* 1991;138:3536–3545.
[189] Hayashi M, Arai H, Ohtsuka H, Sakurai Y. Electrochemical characteristics of calcium in organic electrolyte solutions and vanadium oxides as calcium hosts. *J. Power Sources* 2003;119–121:617–620.
[190] Datta D, Li JW, Shenoy VB. Defective graphene as a high-capacity anode material for Na- and Ca-ion batteries. *ACS Appl. Mater. Interfaces* 2014;6:1788–1795.
[191] Er DQ, Li JW, Naguib M, Gogotsi Y, Shenoy VB. Ti_3C_2 MXene as a high capacity electrode material for metal (Li, Na, K, Ca) ion batteries. *ACS Appl. Mater. Interfaces* 2014;6:11173–11179.
[192] Xu C, Li B, Du H, Kang F. Energetic zinc ion chemistry: the rechargeable zinc ion battery. *Angew. Chem.* 2012;51:933–935.
[193] Zhang GQ, Zhang XG. A novel alkaline Zn/MnO_2 cell with alkaline solid polymer electrolyte. *Solid State Ion.* 2003;160:155–159.
[194] Lee J, Ju JB, Cho WI, Cho BW, Oh SH. Todorokite-type MnO_2 as a zinc-ion intercalating material. *Electrochim. Acta* 2013;112:138–143.
[195] Lee B, Lee HR, Kim H, Chung KY, Cho BW, Oh SH. Elucidating the intercalation mechanism of zinc ions into alpha-MnO_2 for rechargeable zinc batteries. *Chem. Commun.* 2015;51:9265–9268.
[196] Xu C, Du H, Li B, Kang F, Zeng Y. Reversible insertion properties of zinc ion into manganese dioxide and its application for energy storage. *Electrochem. Solid-State Lett.* 2009;12:A61–A65.
[197] Xia H, Lai M, Lu L. Nanoflaky MnO_2/carbon nanotube nanocomposites as anode materials for lithium-ion batteries. *J. Mater. Chem.* 2010;20:6896–6902.
[198] Wang Z, Bramnik N, Roy S, Di Benedetto G, Zunino JL, Mitra S. Flexible zinc–carbon batteries with multiwalled carbon nanotube/conductive polymer cathode matrix. *J. Power Sources* 2013;237:210–214.
[199] Xu D, Li B, Wei C, He Y-B, Du H, Chu X, Qin X, Yang Q-H, Kang F. Preparation and characterization of MnO_2/acid-treated CNT nanocomposites for energy storage with zinc ions. *Electrochim. Acta* 2014;133:254–261.
[200] Zhang B, Liu Y, Wu X, Yang Y, Chang Z, Wen Z, Wu Y. An aqueous rechargeable battery based on zinc anode and $Na_{0.95}MnO_2$. *Chem. Commun.* 2014;50:1209–1211.
[201] Yu X, Fu Y, Cai X, Kafafy H, Wu H, Peng M, Hou S, Lv Z, Ye S, Zou D. Flexible fiber-type zinc–carbon battery based on carbon fiber electrodes. *Nano Energy* 2013;2:1242–1248.
[202] Jia ZJ, Wang BG, Wang Y. Copper hexacyanoferrate with a well-defined open framework as a positive electrode for aqueous zinc ion batteries. *Mater. Chem. Phys.* 2015;149:601–606.
[203] Cheng J, Zhang L, Yang Y-S, Wen Y-H, Cao G-P, Wang X-D. Preliminary study of single flow zinc-nickel battery. *Electrochem. Commun.* 2007;9:2639–2642.
[204] Mirmohseni A, Solhjo R. Preparation and characterization of aqueous polyaniline battery using a modified polyaniline electrode. *Eur. Polym. J.* 2003;39:219–223.
[205] Ghanbari K, Mousavi MF, Shamsipur M, Karami H. Synthesis of polyaniline/graphite composite as a cathode of Zn-polyaniline rechargeable battery. *J. Power Sources* 2007;170:513–519.
[206] Jugović BZ, Trišović TL, Stevanović J, Maksimović M, Grgur BN. Novel electrolyte for zinc–polyaniline batteries. *J. Power Sources* 2006;160:1447–1450.
[207] Xia Y, Zhu D, Si S, Li D, Wu S. Nickel foam-supported polyaniline cathode prepared with electrophoresis for improvement of rechargeable Zn battery performance. *J. Power Sources* 2015;283:125–131.
[208] Jayaprakash N, Das SK, Archer LA. The rechargeable aluminum-ion battery. *Chem. Commun.* 2011;47:12610–12612.
[209] Liu S, Hu JJ, Yan NF, Pan GL, Li GR, Gao XP. Aluminum storage behavior of anatase TiO_2 nanotube arrays in aqueous solution for aluminum ion batteries. *Energy Environ. Sci.* 2012;5:9743–9746.
[210] Liu Y, Sang S, Wu Q, Lu Z, Liu K, Liu H. The electrochemical behavior of Cl^- assisted Al^{3+}insertion into titanium dioxide nanotube arrays in aqueous solution for aluminum ion batteries. *Electrochim. Acta* 2014;143:340–346.
[211] He YJ, Peng JF, Chu W, Li YZ, Tong DG. Black mesoporous anatase TiO_2 nanoleaves: a high capacity and high rate anode for aqueous Al-ion batteries. *J. Mater. Chem. A* 2014;2:1721–1731.
[212] Liu S, Pan GL, Li GR, Gao XP. Copper hexacyanoferrate nanoparticles as cathode material for aqueous Al-ion batteries. *J. Mater. Chem. A* 2015;3:959–962.
[213] Wang W, Jiang B, Xiong WY, Sun H, Lin ZS, Hu LW, Tu JG, Hou JG, Zhu HM, Jiao SQ. A new cathode material for super-valent battery based on aluminium ion intercalation and deintercalation. *Sci. Rep.* 2013;3:3383–3388.
[214] Reed LD, Menke E. The roles of V_2O_5 and stainless steel in rechargeable Al-ion batteries. *J. Electrochem. Soc.* 2013;160:A915–A917.
[215] Wang H, Bai Y, Chen S, Luo X, Wu C, Wu F, Lu J, Amine K. Binder-free V_2O_5 cathode for greener rechargeable aluminum battery. *ACS Appl. Mater. Interfaces* 2015;7:80–84.
[216] Novák P, Müller K, Santhanam K, Haas O. Electrochemically active polymers for rechargeable batteries. *Chem. Rev.* 1997;97:207–282.
[217] Hudak NS. Chloroaluminate-doped conducting polymers as positive electrodes in rechargeable aluminum batteries. *J. Phys. Chem. C* 2014;118:5203–5215.
[218] Mallouk T, Bartlett N. Reversible intercalation of graphite by fluorine: a new bifluoride, $C_{12}HF_2$, and graphite fluorides, C_xF ($5 > x > 2$). *J. Chem. Soc. Chem. Commun.* 1983:103–105.
[219] Rani JV, Kanakaiah V, Dadmal T, Rao MS, Bhavanarushi S. Fluorinated natural graphite cathode for rechargeable ionic liquid based aluminum-ion battery. *J. Electrochem. Soc.* 2013;160:A1781–A1784.